Quantitative CH measurements in atmospheric-pressure, premixed flames of C_1–C_4 alkanes

Philippe Versailles[a], Graeme M.G. Watson[a], Antonio C.A. Lipardi[a], Jeffrey M. Bergthorson[a,*]

[a]*Department of Mechanical Engineering, McGill University*
817 Sherbrooke Street West, Montréal, Québec, Canada, H3A 0C3.

Abstract

The rapid formation of nitric oxide (NO) within the flame front of hydrocarbon flames, occurring via the prompt-NO formation route, is strongly coupled to the concentration of the methylidyne radical, [CH]. This work presents absolute measurements of [CH] taken in atmospheric-pressure, premixed, stagnation flames of methane, ethane, propane, and *n*-butane. One-dimensional (1D) CH fluorescence profiles are extracted from 2D Planar Laser-Induced Fluorescence (PLIF) measurements made quantitative through normalization by the Rayleigh scattering signal of nitrogen. Axial velocity profiles are measured by Particle Tracking Velocimetry (PTV) and, along with mixture composition and temperature measurements, provide the required boundary conditions for flame simulations based on the 1D hydrodynamic model of Kee et al. [1]. A time-resolved, four-level, LIF model considering rotational energy transfer in both the ground and excited electronic states is used to convert the modelled CH concentration profiles into units compatible with the quantitative CH-LIF measurements. Large variations in the CH concentrations predicted by four thermochemical mechanisms are observed for all fuels and equivalence ratios considered. A detailed study of the mechanisms through reaction path and sensitivity analysis shows that the principal reactions impacting CH formation are: a) involved in the CH formation route ($CH_3 \rightarrow CH_2^* \rightarrow CH_2 \rightarrow CH$), b) bypass and remove carbon atoms from the CH formation route, or c) affect the pool of reaction partners in the aforementioned reactions. The order of magnitude variability in the model predictions is caused by significant disagreements among the mechanisms in terms of rate coefficients and reactions included in these pathways. This data set is made available and provides validation and optimization targets for future combustion model revisions.

*Corresponding author, jeff.bergthorson@mcgill.ca

Keywords: alkanes, CH-LIF, LIF modelling, methylidyne, reaction path analysis.

1. Introduction

Increasingly stringent regulations on nitrogen oxides (NO_x) emissions are being enforced by governments owing to their deleterious effects on environment [2]. The principal NO_x produced in combustion processes is nitric oxide (NO). Four NO formation routes have been identified in the combustion of gaseous fuels: thermal (Zel'dovich), prompt, N_2O, and NNH [2, 3]. While the thermal route is generally the dominant formation mechanism in the post-flame region, the prompt route is the source of rapid NO formation through the reaction zone of hydrocarbon flames. The reaction of methylidyne with nitrogen, $CH + N_2 \rightarrow HCN + N$, was initially proposed by Fenimore as the initiation reaction of the prompt-NO route [4]. It was later shown that this reaction is spin-forbidden for reactants and products in the ground electronic state [5, 6], which led Moskaleva and Lin [7] to propose the more probable, spin-allowed reaction $CH + N_2 \rightarrow NCN + H$.

Sutton et al. [8] measured NCN and NO profiles in low-pressure, McKenna burner stabilized, premixed $CH_4/O_2/N_2$ flames. The measured NCN-layer profiles were consistently observed immediately downstream of the CH-layer profiles measured by Berg et al. [9] in an identical burner, and a strong correlation was found between the maximum CH, NCN, and NO concentrations. In a subsequent study considering C_1-C_4 alkanes [10], the same authors showed that the strong correlation between NCN and NO is preserved as the chain-length is increased, but that of CH with NCN weakens. They concluded that there may be another precursor to NCN that becomes increasingly important for longer-chain alkanes. Our research group used laser-induced fluorescence to measure CH and NO concentration profiles in atmospheric-pressure, premixed, stoichiometric and rich stagnation flames of air with C_1-C_4 alkanes and alcohols [11, 12]. For all considered fuels, the results demonstrated a strong correlation between maximum concentrations of NO and CH, if the latter is scaled by the residence time in the flame reaction zone, confirming the primary role of methylidyne as precursor of prompt-NO at atmospheric-pressure. For thermochemical mechanisms to properly describe NO formation, it is then a prerequisite to accurately model the flame reactivity as well as the concentration profile of methylidyne, [CH].

The design of reliable, fully-constrained thermochemical mechanisms requires a comprehensive set of independently-determined experimental data of known, and sufficiently-high, accuracy [13, 14]. With time, a vast pool of experimentally-determined laminar flame speeds was assembled accounting for a variety of operating conditions, types of inert, dilution levels, and fuels [15, 16]. While simple fuels were originally studied, the body of experimental data is now extended to more complex and larger hydrocarbon and oxygenated fuel molecules owing to the recent interest in using non-conventional, fossil and bio-derived fuels [17, 18].

On the other hand, the body of available experimental data is not as exhaustive when it comes to methylidyne concentration, as summarized in Table 1. With few exceptions, experiments were generally performed with methane or also acetylene owing to its intense formation of CH mitigating the need for highly sensitive diagnostics. To the best knowledge of the authors, quantitative [CH] measurements for hydrocarbons longer than acetylene at atmospheric pressure and above are not available in the literature. Furthermore, only a limited number of studies systematically investigated the effect of equivalence ratio, most of them being devoted to partially-, non-premixed, or rich flames.

Proper optimization of thermochemical mechanisms can only be achieved if the experiments can be accurately reproduced numerically. The validation targets, as well as the initial/boundary conditions to the simulation, must be accurate, and their respective uncertainties properly estimated. As shown in Table 1, the McKenna burner is the preferred configuration at low pressure as it produces a flat flame stabilized through heat-loss to the porous surface. It is conveniently solved in modern numerical combustion models assuming one-dimensionality of the reactive flow, and knowing the mixture composition and flow rate, as well as the surface temperature or alternatively the axial temperature profile through the flame front [40]. Due to reduced molecular collision rates at low pressure, the thickness of the CH layer generally spans over several millimetres [9]; hence, highly-spatially resolved measurements are not required and absorption methods involving laser beams of finite diameter can be used. As pressure is increased to more practical conditions, the flame stabilizes closer to the porous surface of the McKenna burner and the thickness of the CH layer decreases. This makes measurements on the reactant side and through the flame front unrealisable, and laser-based diagnostics difficult due to scattering on the burner surface [41]. Hence, a vari-

Table 1: Summary of CH formation data in laboratory flames.

Burner type	Flame type*	Fuel	$\phi^\dagger$	P (atm)	Diagnostic‡	Ref.
McKenna	Pr	CH_4	1.07	0.0332	Lin. LIF + CRDS	[19, 20]
McKenna	Pr	CH_4	0.81,1.07,1.28	0.033, 0.040	Abs. lin. LIF	[9, 21]
McKenna	Pr	CH_4	1.07,1.28	0.033, 0.040	Abs. lin. LIF	[10]
		C_2H_6				
		C_3H_8				
		C_4H_{10}				
McKenna	Pr	C_3H_8	1.15	0.053	Abs. lin. LIF	[20, 22]
McKenna	Pr	C_2H_2	0.6-1.4	0.053, 0.079, 0.13	Laser absorption	[23]
Bunsen	PPr	CH_4	1.36	1	Abs. lin. LIF	[24]
Bunsen	Pr	CH_4	0.85-1.55	1	Rel. sat. LIF	[25]
		C_3H_8				
Bunsen	NPr	CH_4	N/A	1	Abs. lin. LIF	[26]
Counterflow	NPr	CH_4	N/A	1	Abs. lin. LIF	[27]
Counterflow	NPr, PPr	CH_4	1.45,1.6,2.0	1	Lin. LIF + CRDS	[28]
Counterflow	NPr	CH_4	N/A	1	Rel. lin. LIF	[29]
		C_2H_2				
		C_2H_6				
McKenna	Pr	CH_4	1.2	1	CRDS	[30]
Jet-wall	Pr	CH_4	0.69,0.96,1.31	1	Rel. sat. LIF	[31, 32]
Padley-Sugden	Pr	C_2H_2	1.2,1.6,2.0	1	Rel. sat. LIF	[33]
Slot	Pr	C_2H_2	N/Av.	1	Abs. sat. LIF	[34–36]
Torch	Pr	C_2H_2	1.05	1	CRDS	[30]
Wolfard-Parker	NPr	CH_4	N/A	1	CRDS	[37]
Wolfard-Parker	NPr	CH_4	N/A	1	WMS	[38]
		C_2H_2				
Counterflow	NPr, PPr	CH_4	1.45,1.6,2.0	1, 3, 6, 9, 12	Abs. lin. LIF	[39]

* Pr, NPr, and PPr stand for premixed, non-premixed, and partially-premixed flames, respectively.
† N/A and N/Av. stand for not applicable, and not available, respectively.
‡ Abs., Rel., Lin., Sat., LIF, CRDS, and WMS correspond to absolute, relative, linear, saturated, laser-induced fluorescence, cavity ring-down spectroscopy, and wavelength modulation absorption spectroscopy, respectively.

ety of different burners producing partially-, non-, and premixed flames are used at higher pressures. While some configurations, such as the counterflow and jet-wall burners, can be directly simulated invoking quasi one-dimensionality of the hydrodynamics without significant loss of accuracy [1, 42–44], others are simulated with models not exactly reproducing the experiments (e.g., 1D freely-propagating flame approximating a Bunsen flame [25]), or just cannot be simulated using reduced order modelling and instead require more complex CFD computations. In these last two situations, model validation using experimental data is made difficult, and the relevancy to chemistry modellers reduced.

As CH is a short-lived radical, it prevents the use of diagnostic methods relying on mechanical probes and rather requires the use of *in-situ* measurements. Non-intrusive, laser-based

techniques are commonly used to measure the concentration of radicals in flames as discussed in [45, 46]. As shown in Table 1, laser absorption and laser-induced fluorescence (LIF) are common methods to probe CH concentration in flames. Being spatially-resolved, LIF is often preferred to absorption techniques. It consists of exciting the molecules by laser light irradiation and collecting the spontaneous light emission of excited molecules as they return to the ground state. Saturated LIF has the benefit of high signal-to-noise ratio and is insensitive to the rate of collisional quenching of the excited molecules by other species [24]. However, it is plagued with the problem of partial-saturation, both spatially and temporally, due to lower irradiance on the edges of the laser beam and finite rise and fall times of the laser pulse, respectively, causing inaccuracies in the measured CH concentration [24]. Alternatively, linear LIF operating on weak laser irradiation can be used at the expense of reduced signal-to-noise ratio; however, the rate of collisional quenching must be taken into account [24, 45, 46]. While the fluorescence intensity is normalized to a nominal case for relative LIF measurements, absolute (quantitative) LIF requires calibration of the optical collection system. Since CH has a short chemical lifetime, it cannot be stored and seeded in known concentrations for calibration purposes as done for NO-LIF [47–49]. Instead, the CH-LIF signal is generally adjusted to match a quantitative measurement obtained with a different diagnostic technique, such as CRDS [19, 20, 28], or by determining the optical calibration coefficient from Raman [24] or Rayleigh [9, 20–22, 26, 27, 34–36] scattering signals.

Given the current state of knowledge, the objective of this work is to undertake an assessment of the formation of CH in atmospheric-pressure, premixed flames of C_1-C_4 normal alkanes at equivalence ratios, ϕ, ranging from 0.7 to 1.5 to evaluate the current understanding of CH production and the modelling capability of a selection of available thermochemical mechanisms. The paper starts with a survey of the jet-wall stagnation flame apparatus, as well as the Particle Tracking Velocimetry (PTV) and Planar Laser-Induced Fluorescence (PLIF) methods used in this study. Experimentally determined maximum concentrations of CH over a range of equivalence ratios are then presented for each fuel and compared to predictions from four thermochemical mechanisms. A detailed analysis of the mechanisms is also presented to identify the sources of the significant variability observed in predictive performance, and highlight the principal rate coefficients that must be improved to better

capture the experimental data. The measurements reported in this investigation are expected to be useful as targets for the development, optimization, and validation of thermochemical mechanisms.

2. Methodology

2.1. Experimental apparatus

The experiments were performed in an atmospheric-pressure, premixed, jet-wall stagnation burner, a configuration extensively used by our research group, as well as many others, to study flame reactivity [31, 50, 51] and NO formation [11, 12, 47, 48, 52] of fossil and bio-derived fuels. This geometry produces stable, compact, lifted flames readily accessible for optical diagnostics and free from influences from the burner boundaries. As such, the burning rate, flame temperature, and species profiles are functions of the fundamental properties of the combustible mixture. Details on the design, performance, and modelling of the jet-wall stagnation burner are found in [32, 44, 48, 53].

2.1.1. Jet-wall stagnation flame burner

A combustible jet of premixed fuel and air exits a converging nozzle with a throat diameter of 20 mm, and impinges on a water-cooled stagnation plate located $\sim$ 25 mm away from the nozzle assembly. The inner jet decelerates as it approaches the stagnation surface maintained at $\sim$ 350 K to prevent condensation and surface reactions [54], and the flame stabilizes where its propagation speed matches the flow velocity. A co-flowing stream of inert gas, nitrogen or helium depending on flame composition, shrouds the inner jet to insulate the flame from the environment and improve its stability [32]. The temperatures of the plate and inner jet, obtained during and following each experimental trial, respectively, are measured with type-K thermocouples, and the mass flow rates of fuel and air are controlled with thermal mass flow controllers (MFC, Brooks models 5850S and 5851S). The MFC are calibrated using a DryCal ML-500-44 dry-piston calibrator providing a total uncertainty of $\pm$0.45% of the measured mass flow rates, leading to a total uncertainty of $\pm$0.64% in terms of equivalence ratio. The velocity of the inner jet exiting the nozzle is measured via Particle Tracking Velocimetry (PTV) discussed in section 2.2.

2.1.2. Numerical modelling and post-processing

The axisymmetrical nature of the jet-wall configuration allows for simplification of the three-dimensional Navier-Stokes, continuity, and energy and species conservation equations to a quasi one-dimensional (1D) formulation invoking similarity assumptions [1]. The quasi-1D model provides good agreement with experiments in terms of flow velocity, temperature, and species concentration profiles if the velocity boundary conditions (BC) are obtained through a parabolic fit to the velocity data in the un-reacted, stagnating cold flow region (see section 2.2), if the motion of the tracer particles is modelled, and if the thermochemical mechanism describing the chemical rates, thermodynamic and transport properties is accurate [44, 48, 50, 55, 56].

Here, the experiments are numerically reproduced with the premixed, burner stabilized stagnation flame reactor of the Chemkin-Pro software package [40]. This reactor solves the 1D axisymmetrical model of Kee et al. [1] along with the energy and species conservation equations for the following set of boundary conditions: u_{inlet}, $v/r \approx -1/2 \cdot du/dx|_{\text{inlet}}$, T_{inlet}, and $Y_{i,\text{inlet}}$ at the inlet, and T_{wall}, $u = 0$, $du/dx = 0$, and $\rho Y_i(u + V_i) = 0$ at the stagnation surface. The specification of the wall temperature, T_{wall}, accounts for the heat loss to the plate, and the mass transport BC implies no-flux of species at the stagnation surface (surface reactions neglected). The experimentally-determined BC are reported for all cases in Table B1. Mixture-averaged formulation of the diffusion coefficients is used and thermal (Soret) diffusion neglected. Convergence down to 10^{-5} and 10^{-9} in terms of relative and absolute tolerances, respectively, is achieved on meshes refined to achieve *grad* and *curv* parameters of 0.05 and 0.075, respectively.

The predictive capability of four thermochemical mechanisms is studied in this work. GRI-Mech 3.0 (GRI) [57] was assembled to model the combustion of natural gas. It consists of 325 reversible and non-reversible reactions involving 53 species. The rates of the reactions were adjusted using a global optimization procedure against an extensive set of validation targets. Of particular interest for the current study, GRI was validated against methylidyne concentration in low-pressure flames stabilized on McKenna burners [20, 21] and during rich methane oxidation behind shock waves [58].

Another model is the San Diego mechanism (SD) [59] that includes C_1-C_3 hydrocarbon

and C_1-C_2 alcohol chemistry. The 2005 version used here has 235 reactions and 46 species, and does not include the optional NO sub-mechanism. This mechanism, optimized for pressures <100 atm and temperatures >1000 K, differs from the other models by its design philosophy which aims to include the minimum number of species and reactions to describe the combustion processes of interest. An historical perspective on the development of the SD mechanism is presented in [60]. It does not appear that the SD model has been validated against experimental CH measurements; however, the mechanism supplemented with NO chemistry was validated against NO_x measurements obtained with a NO analyzer in counterflow, two-stage methanol [61] and methane flames [62].

A third model is USC Mech II (USC) by Wang et al. [63]. This mechanism describes the high-temperature combustion of H_2, CO, and C_1-C_4 hydrocarbons using 111 species and 784 reactions. It was benchmarked against a comprehensive set of species profiles in shock tubes, flow reactors, and low-pressure flames, but not against CH concentration data.

Recently, new-generation, hierarchical chemical mechanisms were designed to simulate the combustion behaviour of a comprehensive set of fuels over a wide range of regimes by including all relevant reaction steps, regardless of their significance [16, 64]. The AramcoMech 1.3 mechanism (NUIG) [64] was constructed in a hierarchical manner, starting with simple, short-chain fuels to more complex C_1 to C_4 hydrocarbon and oxygenated chemistry. This model contains 253 species and 1542 reactions, and has been validated against numerous experimental targets including species concentrations in jet-stirred and flow reactors, but not against [CH] measurements.

Reaction Path Analysis (RPA) is a useful tool to visualize and understand the complex chemistry included in modern thermochemical models. The RPA outputs a network where the nodes are chemical species linked together by arrows representing the chemical reactions. The RPA method used here is inspired by [65] where a conserved scalar, the flux of element e, is tracked as reactants are made into products. The thickness of the arrows in the network are linearly scaled with the spatially-integrated rate of transfer of element e from species s_1 to s_2, $R(e, s_1, s_2)$ (kmole/s), calculated using equation (1) where $n_l(e, s_1, s_2)$ is the number of atoms of element e transferred from species s_1 to s_2 through reaction l, $q_l(x)$ (kmole/m^3-s) is the rate of progress variable of reaction l, x [m] is the axial direction, and r [m] is

the radius of the cylindrical control volume (CV) adjusted to achieve an influx of element e of 1 kmole/s. As such, $R(e, s_1, s_2)$ can be thought of as an absolute flux of element e, or as a fraction of the flux of e-atoms entering the control volume. To prevent molecular transport fluxes across the CV boundaries, x_i and x_f, the inlet and outlet locations of the control volume, respectively, are taken at the inlet and outlet of the numerical computational domain. Then, the net flux of element e crossing the boundaries of the CV is determined solely from the mixture composition, velocity, and density data commonly available in the output of combustion simulations.

$$R(e, s_1 s_2) = \int_{x_i}^{x_f} \sum_{l} n_l(e, s_1, s_2) \cdot q_l(x) \cdot \pi r^2 \, \mathrm{d}x \tag{1}$$

Equation (1) differs from [65] by the summation over all l reactions being inside of the spatial integral. This allows for a significant reduction in the number of numerical integrations performed and, thereby, provides a reduced numerical error in calculating $R(e, s_1, s_2)$. The integration is performed using a Simpson's 1/3 rule re-developed in this work to make it applicable to unequally distributed grid points characteristic of refined computational meshes.

2.2. Particle Tracking Velocimetry (PTV)

The velocity boundary conditions are obtained through Particle Tracking Velocimetry (PTV). This Lagrangian technique consists of recording the trajectory of individual tracer particles illuminated by a laser source, and subsequently converting the spatio-temporal information to velocities, and their derivatives. Two- and stereoscopic three-dimensional PTV methods, with particle streaks obtained from single images or a set of consecutive images, have been used to study droplet atomization [66], the geological phenomenon of saltation [67], turbulent flows [68], and laminar combustion [56, 69, 70]. Simulations have demonstrated that small-size inert particles act as a diluent in particle-laden premixed flames causing a monotonic reduction of flame temperature and speed as the particle loading is increased [71]. The main benefit of PTV for the current study is to reduce this thermodynamic effect by theoretically requiring a particle loading as much as five orders of magnitude lower than other common techniques, such as PIV.

The PTV method used in this study extends the work of Benezech et al. [56, 70]. The inlet flow is seeded with a minimal amount of refractive scattering particles (1μm diameter

Al_2O_3 particles) illuminated by a high repetition rate, diode pumped, dual cavity Nd:YLF laser (Litron LDY 303, $\lambda = 527$ nm, 20 mJ/pulse at 1kHz). For the current set of experiments, the laser is operated at a repetition rate, f, of 8 kHz adjusted to maximize the resolution of the measurements in the low velocity region immediately upstream of the flame. Using a series of plano-spherical and plano-cylindrical borosilicate (N-BK7) glass lenses, the beam emerging from the laser is made into a ~ 1 mm thick sheet centred on the axis of the burner. The light scattered by the particles is collected using a 90 mm Tamron f/2.8 macro lens, and focused on a 14-bit monochrome, CCD camera (Cooke PCO.2000, 2048×2048 pixels^2). An exposure time of 150 ms results in a series (streaks) of dots, analogous to streamlines, on individually captured images (see Salusbury and Bergthorson [72]). The exact location of the dots is obtained through a grey scale intensity centroid calculation in the image frame, and made dimensional by applying a calibration factor obtained from an image of a dotted-target of known grid-size. Invoking the Lagrangian description of the flow, the particle velocity, $u_\mathrm{p}(x)$, is recovered from the time history of the particles using a second-order, central finite difference scheme.

Particle velocimetry methods rely on the assumption that the particles closely track the flow. However, it has been shown that high-gradient, high-curvature, chemically reactive flows are plagued by significant particle lag due to the combined effects of the thermophoretic force and particle inertia [55, 73, 74]. Since the boundary conditions for the simulations are measured 1.5 mm upstream of the reaction zone, the temperature is approximately constant and equal to the inlet (cold) temperature, and the rate of flow deceleration is weak enough, that the particles accurately track the flow. When simplified by assuming an isothermal fluid, the analytical solution of the quasi-1D hydrodynamic model of Kee et al. [1] is a second-order polynomial [31, 32]. The inlet velocity BC is then obtained by a least-squares fit of a parabola to the cold, constant-temperature portion of the velocity profile made from the superposition of 15 to 30 post-processed streaks. Considering the parabolic nature of the flow velocity profile, the first-order velocity derivative is obtained by a least-squares linear regression to $du_\mathrm{p}/dx(x)$. The experimental values of the velocity derivative are obtained using equation (2), which includes a second-order, central finite difference to approximate the derivative of $\ln(u)$. Through error analysis, this method was proven more accurate than

taking the derivative of the parabola adjusted to the velocity data.

$$\frac{du}{dx} = \frac{du}{dt}\cdot\frac{1}{u} = \frac{d\ln(u)}{dt} \approx \{\ln[u(t+1/f)] - \ln[u(t-1/f)]\}\cdot f = \ln\left(\frac{u(t+1/f)}{u(t-1/f)}\right)\cdot f \tag{2}$$

2.3. Two-Dimensional CH *Laser-Induced Fluorescence*

The current work uses two-dimensional CH-LIF made quantitative through normalization by the Rayleigh scattering signal of nitrogen. Traditionally (e.g., [26]), the optical calibration coefficient is extracted from an experimentally measured Rayleigh signal and applied to a LIF model to yield the number density of the probed species. This methodology has drawbacks. Namely, the accuracies of the optical calibration and of the conversion of LIF signal intensities into number densities are limited by the accuracy of the models used, and of the temperature and species concentration data they require. In addition, if these models are proven inadequate or improved, it makes the experimental data obsolete even if the methodology is formally correct. To avoid these issues, the approach proposed by Connelly et al. [75] is employed in which relatively raw experimental signals are directly compared to modelled LIF and Rayleigh signal intensities. Experimental and computational parameters are then segregated, removing uncertainties related to the LIF and Rayleigh models from the experimental data.

2.3.1. Experimental procedure

The third-harmonic (355 nm) of a Nd-YAG Laser (Spectra-Physics Quanta-Ray Pro-230) firing at 10 Hz pumps a wavelength-tunable dye laser (Sirah Cobra-Stretch SL) filled with Stilbene 420 dye. A fairly homogeneous portion of the emerging beam is passed through a pinhole iris followed by Powell and plano-cylindrical lenses to form an unfocused, quasi-homogeneous, laser sheet of ∼20 mm by ∼6 mm centred on the axis of the burner. The average energy of the laser sheet is ∼ 0.137 mJ spread over a pulse duration of 8.5 ns. Linearity of the LIF response is ensured by comparison of experimentally realized excitation spectra to theoretically determined ones in LIFBASE [76], and by noting that the spectral irradiance ($I_\nu \approx 3.9\cdot 10^4$ W/(cm^{2}cm^{-1})) is approximately one order of magnitude lower than the value of I_ν at which saturation effects appear [34].

Similarly to other studies [26, 34], the dye laser wavelength is adjusted to ∼426.93 nm

to excite the R(7) ($N'' = 7$, $N' = 8$) transition of the $A^2\Delta$-$X^2\Pi(\nu'' = 0, \nu' = 0)$ system. Λ-doubling and spin-splitting, related to the two possible orientations of the projection of the orbital and spin angular momenta on the internuclear axis, make the ground and excited states degenerate leading to multiple allowed transitions between the two electronic energy states [34]. Figure 1 shows the absorption spectrum of the R(7) A-X(0,0) system as obtained from LIFBASE for a thermalized system at 1800 K (*e* and *f* refer to Λ-doubling, and 1 and 2 to spin-splitting). The spectrum includes the effects of Doppler and collisional line-broadening through convolution of Gaussian and Lorentzian distributions, respectively, with the non-broadened absorption spectrum. Doppler broadening is readily described as it depends only on the gas temperature and molecular mass of the probed species [45, 76]. In contrast, the width of the Lorentzian distribution, calculated using equation (3) where P_i [atm] is the partial pressure of the broadening species i, and $2\gamma_{\mathrm{CH}-i}$ [cm^{-1}/atm] is the collisional broadening parameter [77], depends on the local gas composition, temperature and pressure. Functions describing $2\gamma_{\mathrm{CH}-i}(T)$ for various broadening species are sparse. Vasudevan et al. [78] measured $2\gamma_{\mathrm{CH}-\mathrm{N}_2}(2312\mathrm{K}) = 0.044$ cm^{-1}/atm in an ethane-nitrogen mixture heated by a shock wave. Noting that the mixtures consist mostly of nitrogen in the current set of experiments and applying the temperature dependence of $2\gamma_{\mathrm{OH}-\mathrm{N}_2}(T)$ [77] as performed in [78], the width of the Lorentzian distribution is approximated as $\Delta\nu_c \approx 2\gamma_{\mathrm{CH}-\mathrm{N}_2}(T) \cdot P \approx 0.044 \cdot (\frac{2312}{T})^{0.72} \cdot P$. At 1800 K and 1 atm, this yields $\Delta\nu_c = 0.053$ cm^{-1}, which is in fair agreement with reported values ranging from 0.03 cm^{-1} to 0.1 cm^{-1} at atmospheric-pressure conditions [24, 45].

$$\Delta\nu_c = \sum_i 2\gamma_{\mathrm{CH}-i}(T) \cdot P_i \tag{3}$$

Also shown in Figure 1 is the laser line profile approximated by a Voigt distribution. It was obtained via a least-squares adjustment of a virtual excitation spectrum, made through a convolution of an adjustable Voigt line-shape profile with a theoretical excitation spectrum extracted from LIFBASE including Doppler and collisional line-broadening mechanisms, to an experimentally measured excitation spectrum. Given the thin line width (0.34 cm^{-1}) of the dye laser, the current LIF excitation scheme targets only one spectral feature that includes the $R_{1e}(7)$ and $R_{21e}(7)$ transitions. It must be noted that the Einstein coefficient for

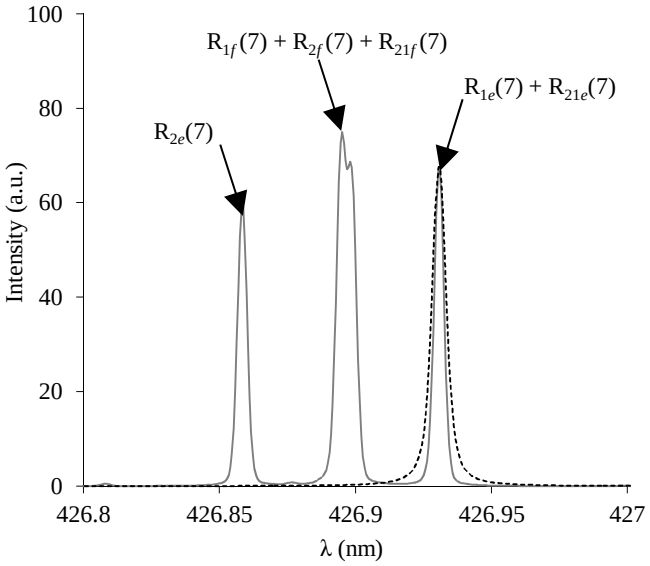

Figure 1: Absorption spectrum of CH at 1800 K assuming thermalized Boltzmann population distribution and accounting for Doppler and collisional line-broadening (solid grey line), superimposed with the laser line profile (black dashed line).

photo absorption, B_{12}, is approximately 50 times larger for the $R_{1e}(7)$ transition.

An off-resonance signal (Figure 2 (b)), measured at a theoretical absorption minimum at 427 nm, is subtracted from the on-resonance signal (Figure 2 (a)) to remove the effect of Rayleigh scattering, ambient luminosity, camera dark noise, and flame chemiluminescence (see net PLIF signal in Figure 2 (c)). Both signals pass through a 10 nm bandpass filter centred at 430 nm (Andover Optics 430FS10-50), and are collected using a 90 mm Tamron f/2.8 macro lens mounted on extension tubes for improved spatial resolution. The signals are recorded using an intensified CCD camera (Dicam Pro, GaAsP photocathode) binned 4 by 4 for increased signal-to-noise ratio (S/N), which results in a projected pixel resolution of 0.029 mm/pixel. 500 images are exposed for 30 ns, a gate time longer than the fluorescence duration but short enough to minimize noise, again in an attempt to boost S/N. One-dimensional profiles of LIF signal intensity are obtained by averaging, at each axial location, the intensity of 50 pixels in the radial direction (see Figure 2 (c & d)).

To yield quantitative data, the LIF signal is normalized by the Rayleigh scattering signal of nitrogen (S_R) measured at the on-resonance laser wavelength using the exact same optical collection configuration. A signal, S_{N_2}, is first recorded with nitrogen gas flowing in the apparatus. Taking advantage of the fact that the Rayleigh scattering cross section of helium

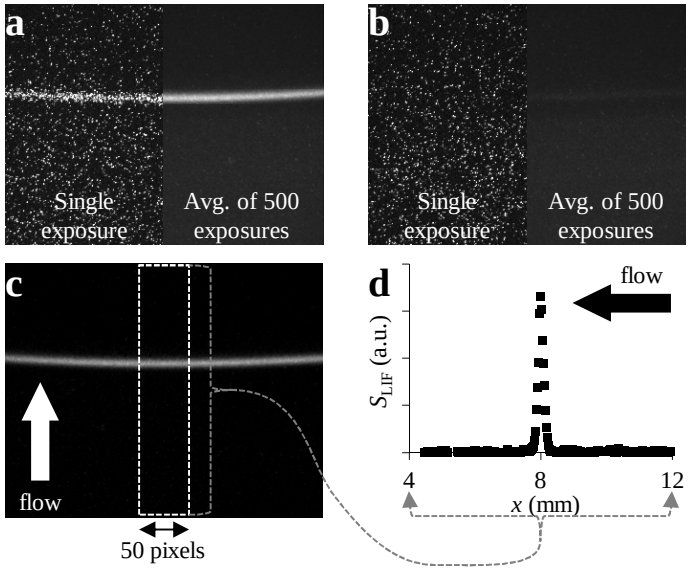

Figure 2: (a) On-resonance PLIF, (b) off-resonance PLIF, (c) net (on − off-resonance) PLIF, and (d) resulting 1D CH-LIF profile. In images (a) and (b), the left and right sides show a single image and the average of 500 exposures, respectively.

is only ∼1.3% that of nitrogen at room temperature and pressure, a Rayleigh signal measured with He is deducted from S_{N_2} to remove the effect of ambient luminosity and camera dark noise ($S_R = S_{N_2} - S_{He}$). To minimize the impact of Mie scattering, the calibration gases are passed through an ultra-high purity particulate filter (Swagelok SS-SCF3-VR4-P-30).

2.3.2. Laser Induced Fluorescence modelling

In LIF data reduction, it is common practice to apply a two electronic energy level model, either in the linear [26] or saturated [34] regimes, motivated by its relative simplicity. For such a model to be accurate, rotational energy transfer (RET) in the ground and electronically-excited states must be either frozen, or extremely fast, resulting in a fully-equilibrated Boltzmann distribution across the rotational energy levels [45]. However, most actual LIF processes at atmospheric pressure present a finite rate of rotational relaxation and RET must be modelled [24, 45]. Furthermore, the achievement of steady-state (SS) conditions is often assumed in the quest of a simple algebraic equation relating the LIF signal intensity to the number density of the probed species. However, the applicability of such an assumption cannot be taken for granted for short-duration, low-intensity laser irradiation and/or slow transitional processes [79].

For these reasons, the current study relies on a time-resolved, four-level LIF model shown

in Figure 3 and developed based on [45]. Each electronic state includes a rotational energy level directly coupled to laser irradiation (state a) and a manifold containing all the other energy levels (state b). The transitions considered in the model are photon absorption (b_{1a2a}), stimulated (b_{2a1a}) and spontaneous (A_{2i1j}) emissions, collisional quenching (Q_{2i1j}), and rotational energy transfer (R_{kakb}, R_{kbka}), while predissociation and photoionization in the electronically-excited state are neglected. Vibrational and electronic energy transfers are also considered negligible in comparison to RET [80]. Upon simplification and invoking species conservation, ODEs describing the rate of change of the population in each of the energy levels are developed, and solved using the Runge-Kutta $4^{\text{th}}/5^{\text{th}}$ order solver of Matlab (version R2011a). The parameters required to assemble the time-resolved, four-level LIF model, which is covered in detail elsewhere [79], are presented in Appendix A.

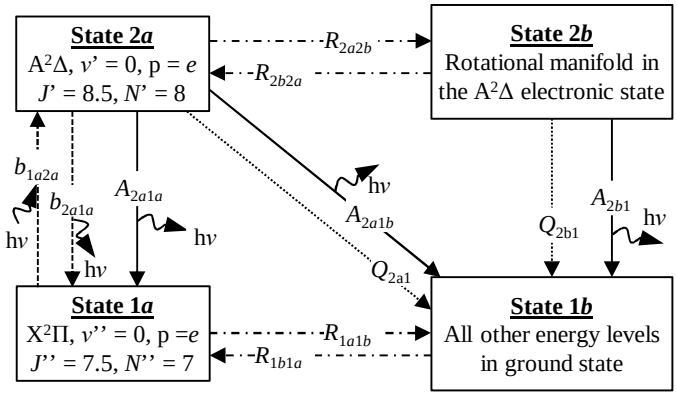

Figure 3: Time-resolved, four-level LIF model.

In order to obtain the LIF signal as recorded by the camera, equation (4) was derived based on the theory presented in [45]:

$$S_{\text{LIF}} = \int_0^{\tau_{\text{cam}}} \sum_{i,j} N_{2i}(t) \cdot A_{2i1j}\, \mathrm{d}t \cdot \frac{\Omega}{4\pi} \cdot V \cdot C_{\text{opt}} \cdot \tau_{\lambda,\text{LIF}}, \tag{4}$$

where S_{LIF} [count] is the LIF signal intensity, τ_{cam} [s] is the camera exposure time, Ω [sr] is the solid angle, V [m^3] is the probed volume, C_{opt} [count/photon] is the optical collection constant, and $\tau_{\lambda,\text{LIF}}$ is the average transmissivity of the bandpass filter over the emission spectrum. The Rayleigh scattering signal is modelled as:

$$S_{\text{R}} = \left[\left(\frac{\partial \sigma}{\partial \Omega} \right)_{\text{N}_2} - \left(\frac{\partial \sigma}{\partial \Omega} \right)_{\text{He}} \right] \cdot N \cdot \frac{I \cdot \tau_{\text{R}}}{h\nu} \cdot \Omega \cdot V \cdot C_{\text{opt}} \cdot \tau_{\lambda,\text{R}}, \tag{5}$$

where S_{R} [count] is the Rayleigh signal intensity, $\left(\frac{\partial\sigma}{\partial\Omega}\right)$ [$\mathrm{m^2/sr}$] is the Rayleigh scattering cross-section calculated according to [81], N [$\mathrm{m^{-3}}$] is the number density, I [$\mathrm{W/m^2}$] is the irradiance, τ_{R} [s] is the duration of the Rayleigh scattering signal corresponding in practice to the laser pulse temporal width, $h\nu$ [J] is the energy of a photon, and $\tau_{\lambda,\mathrm{R}}$ is the transmissivity of the bandpass filter at the on-resonance wavelength. It is assumed that Ω, V, and C_{opt} are equal in equations (4) and (5), which implies that these optical parameters do not appear in modelled $S_{\mathrm{LIF}}/S_{\mathrm{R}}$ ratios. An assessment of the uncertainty of the parameters included in the model coupled with a Monte-Carlo analysis of the system using 50,000 samples provided an estimated accuracy for $S_{\mathrm{LIF}}/S_{\mathrm{R}}$ of $[-23\%; 35\%]$ (95% confidence level), as reported in [79].

At atmospheric pressure, CH exists in a thin, sub-millimetric layer. Due to the effects of diffraction and possible aberrations introduced by the collection optics [82], the measured width of the CH-LIF profile is generally larger than the actual CH layer thickness [27, 31, 32]. To account for imaging-system blur, the simulated LIF profiles are corrected through convolution with a point-spread function (PSF), which is an intrinsic property of the light collection setup [82]. The PSF is theoretically described by the Airy distribution, which can be accurately approximated using a Gaussian distribution [83] normalized so as to conserve the radiant energy of the LIF signal. The full width at half maximum of the PSF ($\delta_{\mathrm{PSF}} = 0.124 \pm 0.009$ mm) was determined by taking the average of the width of the Gaussian PSF-distributions needed to reconcile the CH-LIF layer thicknesses predicted by the four mechanisms with the experimental data obtained in the same apparatus for the stoichiometric, preheated ($T_{\mathrm{inlet}} = 355$ K), CH_4-air flame presented in [11]. This methodology assumes that the thermochemical mechanisms accurately predict the width of the CH layer, hence the reaction zone thickness, of stoichiometric methane-air flames. From flame theory [84], the reaction zone thickness (l_R) is known to be directly and inversely proportional to the thermal diffusivity (α) and flame speed (S_{L}), respectively ($l_R \propto \alpha/S_{\mathrm{L}}$). Considering the demonstrated adequacy of most modern thermochemical mechanisms at predicting the flame speed of stoichiometric CH_4-air mixtures [16, 17, 64], it is expected that both S_{L} and α are properly modelled, and that the CH layer thickness is accurately predicted for methane-air flames at $\phi = 1$.

Figure 4 presents raw (uncorrected, grey dashed curves) and PSF-corrected (solid grey

curves) numerical $S_{\mathrm{LIF}}/S_{\mathrm{R}}$ profiles for lean n-butane, stoichiometric methane, and rich ethane-air flames obtained with the USC, GRI and SD mechanisms, respectively. Absolute LIF profiles are shown in the upper part of the figure (plots a-c), and profiles normalized by the maximum value of $S_{\mathrm{LIF}}/S_{\mathrm{R}}$ are shown in the lower row (plots d-f) to better assess the shape of the profiles. The consistent underprediction of the LIF profile thickness is clearly observed in Figure 4 (d-f) where the uncorrected simulated data lie within the experimentally measured profile (solid squares) for all considered flames. Correcting for the blurring effect induced by the collection optics significantly improves the numerical predictions with the PSF-corrected profiles almost perfectly agreeing with the experimental data.

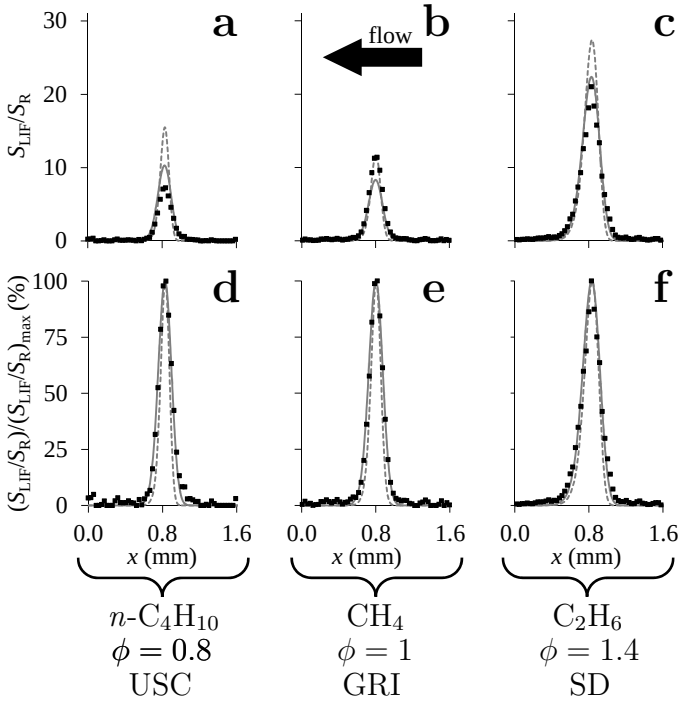

Figure 4: Absolute (top) and normalized (bottom) axial profiles of LIF-to-Rayleigh ratio for $\phi = 0.8$ n-butane, $\phi = 1.0$ methane, and $\phi = 1.4$ ethane flames simulated with the USC, GRI and SD mechanisms, respectively. Flow from right to left. Legend: ■ exp., ------ PSF-uncorrected (raw) numerical profiles, and —— PSF-corrected numerical profiles.

In addition to its broadening effect, the PSF-correction reduces the amplitude of the $S_{\mathrm{LIF}}/S_{\mathrm{R}}$ profiles as shown in Figure 4 (a-c). The effect is particularly pronounced for thin flames; the thinner the flame, the larger the reduction in the peak value of $S_{\mathrm{LIF}}/S_{\mathrm{R}}$ induced by the PSF correction. For the stoichiometric-methane and lean-butane flames (plots b & a), including the point-spread function brings the simulated profiles in closer and almost perfect agreement with the experiments, respectively. For the rich ethane-case, it could be

concluded from the uncorrected data that the SD mechanism exactly predicts CH formation. However, the PSF-corrected profile instead indicates that this model slightly underpredicts the maximum value of $S_{\mathrm{LIF}}/S_{\mathrm{R}}$ in comparison to the experiments. These results demonstrate the necessity to perform the PSF-correction in the reduction of flame simulations into LIF signals to properly assess the predictive capability of thermochemical mechanisms. This is true not only on a quantitative basis, but also in terms of the relative trend of $S_{\mathrm{LIF}}/S_{\mathrm{R}}$ vs. ϕ as the amplitude of the correction depends on the flame thickness, which varies with the equivalence ratio as seen in Figure 4 and discussed below.

3. Results and discussion

3.1. Experimental results and comparison to flame simulations

The Rayleigh-calibrated LIF diagnostic allows for an assessment of the accuracy of different thermochemical mechanisms in predicting CH formation. Although spatial profiles are measured and simulated, it is more convenient to make the comparison using a single scalar value obtained from the CH-LIF profiles. Here, the maximum signal intensity has been selected as a measure of CH production.

Figure 5 presents a comparison of measured and predicted $S_{\mathrm{LIF}}/S_{\mathrm{R}}$ ratios (note the logarithmic scale). The error bars, obtained using the Student's t-distribution, correspond to a 95% interval of confidence for the variability in the measurements. CH production has a similar dependence on equivalence ratio for the four fuels considered in this study, suggesting that fuel-independent elementary reactions dominate CH production in these flames. For all fuels, the LIF signal reaches its maximum at $\phi = 1.2$, and monotonically decreases on both sides of the peak. The models generally capture the relative trend of the data, but predict a larger drop in $S_{\mathrm{LIF}}/S_{\mathrm{R}}$ as the stoichiometry is shifted to lean mixtures (except USC for CH_4-air flames) as also observed in [25, 32]. Simulations performed with the SD mechanism and post-processed with the RPA showed that under lean conditions most of the carbon entering the system is made into methyl that reacts with atomic and molecular oxygen to form formaldehyde subsequently transformed in HCO, CO and CO_2 through the main fuel breakdown route. As the equivalence ratio is increased, the oxygen content in the mixture is depleted and a larger fraction of the carbon goes into forming CH rather than reacting through the main fuel breakdown route. In addition, the methylidyne formed is diluted in

a smaller amount of inert and un-reacted oxygen. Both of these effects combine to raise the maximum number density of CH as the equivalence ratio is increased. However, at sufficiently large values of ϕ, competing rich pathways producing higher-order hydrocarbons, and bypassing carbon away from the CH formation route, become dominant and reduce the LIF-to-Rayleigh ratio beyond $\phi = 1.2$. Through saturated, relative LIF measurements in an atmospheric-pressure Bunsen burner, Sutton and Driscoll [25] found that the maximum CH-LIF signal for methane-air premixed flames occurs at $\phi = 1.25$, which is consistent with the current set of data. In contrast, they observed peak CH-LIF signal intensity at $\phi = 1.35$ for propane-air flames. Considering the width of the error bars reported with their measurements, it is possible that the maximum LIF intensity occurs at $\phi = 1.25$, in better agreement with the present work.

For all fuels and equivalence ratios, there is significant variability in the predictions of the thermochemical mechanisms. The simulated values of $S_{\mathrm{LIF}}/S_{\mathrm{R}}$ are spread over more than an order of magnitude indicating substantial differences in the chemistry (rate coefficients and/or included reactions) of the models. In increasing order of LIF-to-Rayleigh ratio, the mechanisms are generally sorted as NUIG, SD, GRI and USC, no matter the fuel. The kinetic rates governing this ordering, hence the variability in the predictions, must then be related to fuel-independent elementary reactions.

To assess the agreement of the simulations with the experiments, Figure 6 shows the simulated LIF-to-Rayleigh ratios normalized by their experimental counterpart at each equivalence ratio. Exact agreement of the numerical predictions with the experimental data would yield a value of $(S_{\mathrm{LIF}}/S_{\mathrm{R}})_{\mathrm{num}} \,/\, (S_{\mathrm{LIF}}/S_{\mathrm{R}})_{\mathrm{exp}}$ equal to unity (dashed lines). The shaded grey area superimposed on Figure 6 corresponds to the uncertainty in $(S_{\mathrm{LIF}}/S_{\mathrm{R}})_{\mathrm{num}} \,/\, (S_{\mathrm{LIF}}/S_{\mathrm{R}})_{\mathrm{exp}} = 1$, and accounts for the scatter in the experimental data ($\sigma_{(\mathrm{S_{LIF}/S_R})_{\mathrm{exp}}}$, also presented in Figure 5 as error bars), the error in the LIF model ($\sigma_{(\mathrm{S_{LIF}/S_R})_{\mathrm{num}},\mathrm{LIFmodel}}$, see section 2.3.2), as well as the error induced in the LIF response by the uncertainties in the PSF-width and in the experimentally-measured boundary conditions ($\sigma_{(\mathrm{S_{LIF}/S_R})_{\mathrm{num}},\mathrm{B.C.}+\delta_{\mathrm{PSF}}}$, see sections 2.1.2 and 2.3.2). The uncertainties in the PSF-width and in each of the BC are assumed to be statistically independent and their combined contribution to the uncertainty of $(S_{\mathrm{LIF}}/S_{\mathrm{R}})_{\mathrm{num}}$ is taken as $\sigma_{(\mathrm{S_{LIF}/S_R})_{\mathrm{num}},\mathrm{B.C.}+\delta_{\mathrm{PSF}}} = \sqrt{\sum \left[\mathrm{L.S.}(x_j) \cdot \sigma_{x_j}\right]^2}$, where $\mathrm{L.S.}(x_j)$ corresponds to the logarith-

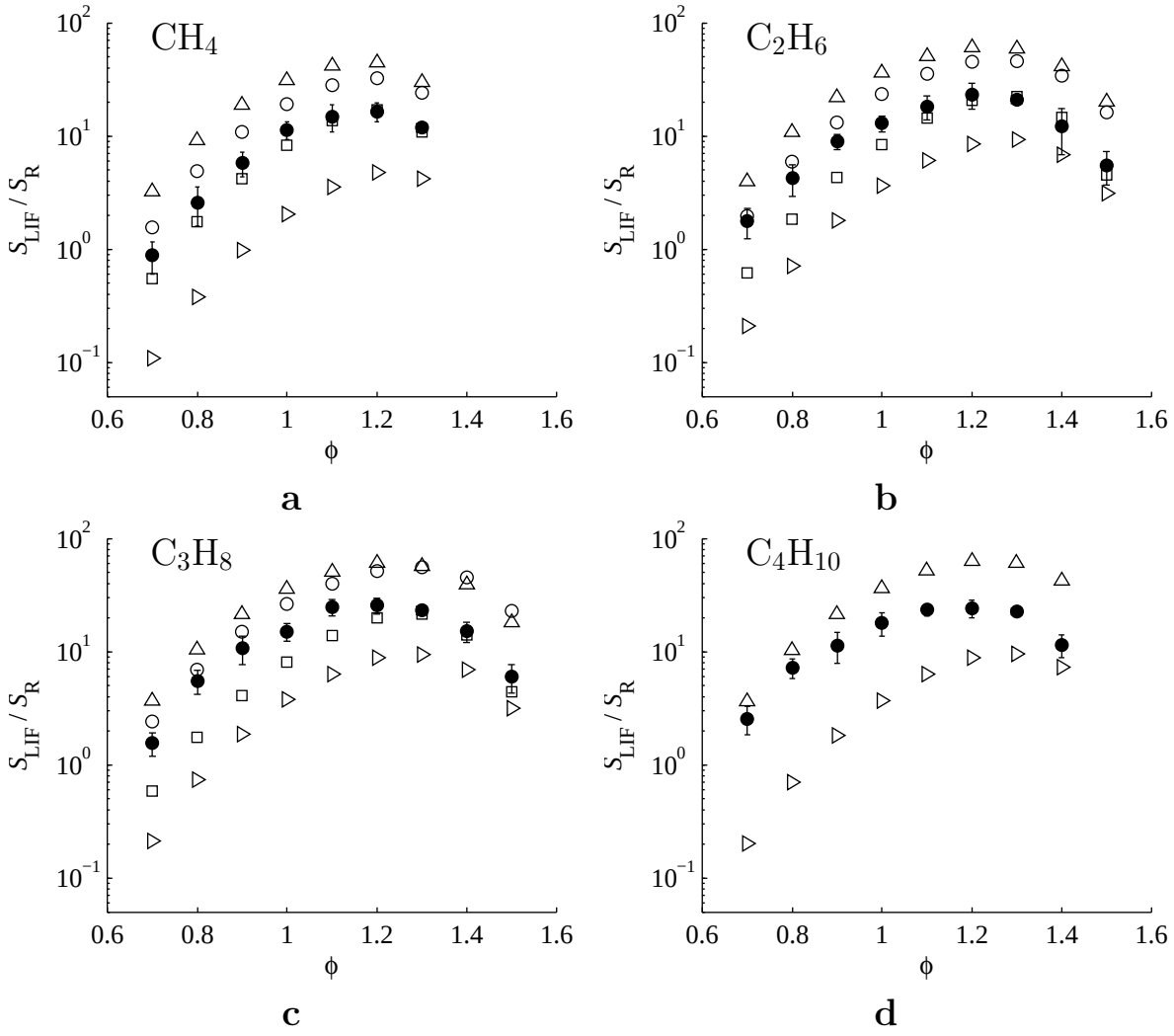

Figure 5: Measured and simulated values of maximum $S_{\mathrm{LIF}}/S_{\mathrm{R}}$ for (a) methane, (b) ethane, (c) propane, and (d) n-butane flames. Legend: • exp., ○ GRI, □ SD, △ USC, and ▷ NUIG.

mic sensitivity of $(S_{\mathrm{LIF}}/S_{\mathrm{R}})_{\mathrm{num}}$ to the parameter x_j obtained through brute-force sensitivity analysis, and σ_{x_j} is the uncertainty in the parameter x_j. Again assuming statistical independence of the individual uncertainties, the overall error in $(S_{\mathrm{LIF}}/S_{\mathrm{R}})_{\mathrm{num}} / (S_{\mathrm{LIF}}/S_{\mathrm{R}})_{\mathrm{exp}} = 1$ is calculated using equation (6), where the last term in the square-root is of minor importance in comparison to the random error in the experimental data and the uncertainty of the LIF model.

$$\sigma_{(\mathrm{S_{LIF}/S_R})_{\mathrm{num}}/(\mathrm{S_{LIF}/S_R})_{\mathrm{exp}}=1} = \sqrt{\sigma^2_{(\mathrm{S_{LIF}/S_R})_{\mathrm{exp}}} + \sigma^2_{(\mathrm{S_{LIF}/S_R})_{\mathrm{num}},\mathrm{LIFmodel}} + \sigma^2_{(\mathrm{S_{LIF}/S_R})_{\mathrm{num}},\mathrm{B.C.}+\delta_{\mathrm{PSF}}}} \quad (6)$$

As observed in Figure 6, the GRI mechanism provides the best overall representation of

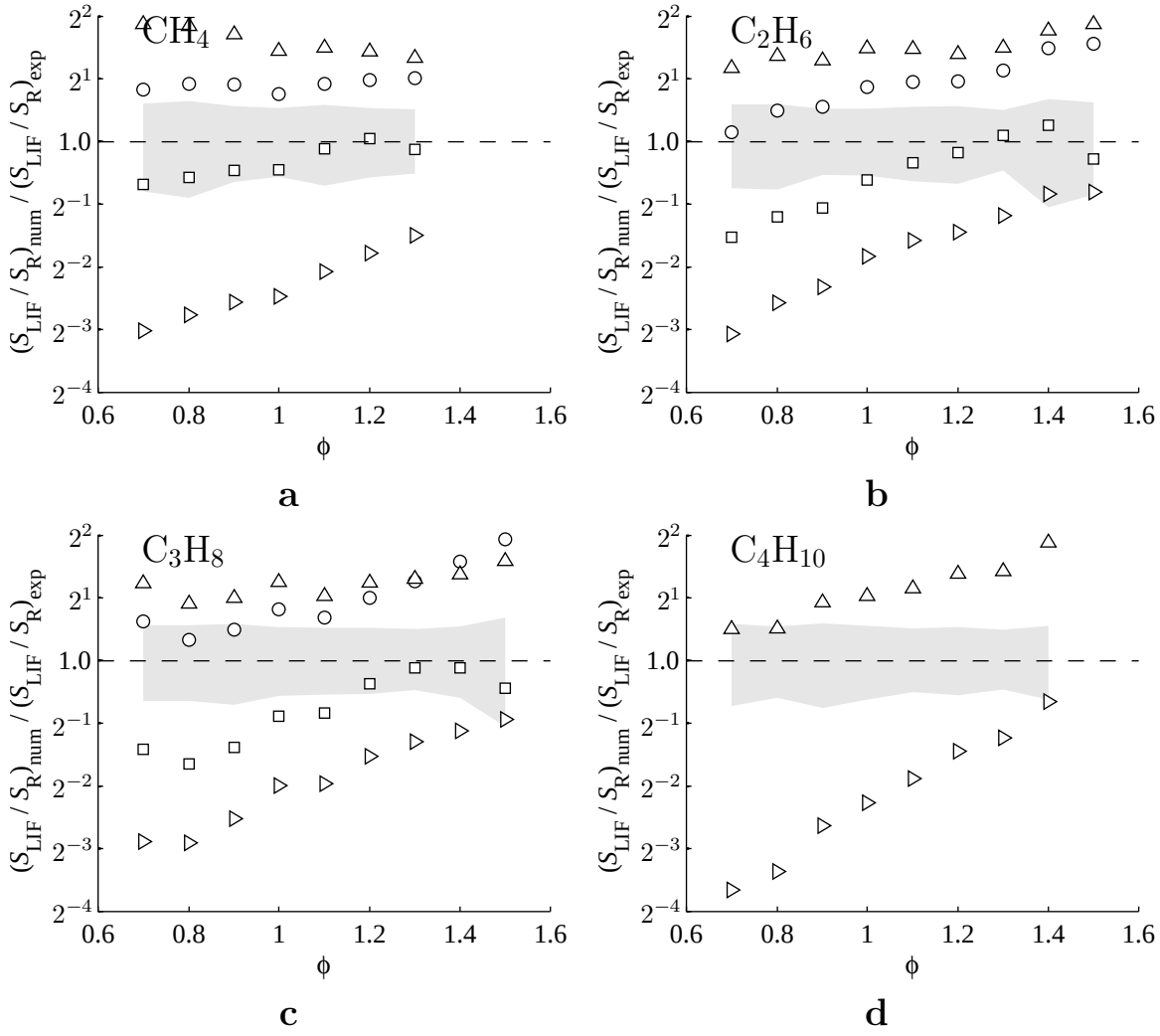

Figure 6: Numerical $S_{\mathrm{LIF}}/S_{\mathrm{R}}$ normalized by the experimental value for (a) methane, (b) ethane, (c) propane, and (d) n-butane flames. $(S_{\mathrm{LIF}}/S_{\mathrm{R}})_{\mathrm{num}} \,/\, (S_{\mathrm{LIF}}/S_{\mathrm{R}})_{\mathrm{exp}} = 1$ shown by dashed lines indicates exact agreement of the predictions with experimental data. The shaded grey bands present the uncertainty resulting from the LIF model, δ_{PSF}, flame boundary conditions and scatter in the measurements. Same legend as Figure 5.

CH formation with $(S_{\mathrm{LIF}}/S_{\mathrm{R}})_{\mathrm{num}} \,/\, (S_{\mathrm{LIF}}/S_{\mathrm{R}})_{\mathrm{exp}}$ agreeing, within uncertainty, with the exact value of 1 for most cases, namely for $\phi \leqslant 1.1$ (1.2 for C_2H_6). However, for richer mixtures, GRI increasingly overpredicts the experimental LIF-to-Rayleigh ratio beyond uncertainty, particularly for ethane and propane flames. It is noteworthy that GRI gives excellent agreement with the experimental data for C_3H_8 flames at $\phi \leqslant 1.1$ even if it was not optimized for propane combustion and contains only a minimal set of C_3 reactions. This again suggests that CH formation is mainly determined by fuel-independent elementary reactions. The SD and NUIG mechanisms are found to consistently underpredict the experiments by as much

as 76% and 94%, respectively. Their predictive capability improves as the equivalence ratio is increased, with the SD model agreeing, within uncertainty, with the experimental data for a few rich flames. On the other hand, the USC mechanism overestimates CH formation by as much as 174%, except for lean-butane flames where the predicted and measured LIF-to-Rayleigh ratios are in very good agreement. Since, for all models, there are cases in Figure 6 for which $(S_{\mathrm{LIF}}/S_{\mathrm{R}})_{\mathrm{num}} \,/\, (S_{\mathrm{LIF}}/S_{\mathrm{R}})_{\mathrm{exp}}$ departs from unity significantly beyond the estimated uncertainty, the current CH-LIF measurements are a suitable data set for optimization of thermochemical mechanisms.

The LIF diagnostic also permits an assessment of the CH profile thickness, δ_{CH}, which is an important parameter determining NO formation through the prompt (Fenimore) route [12]. Figure 7 shows a comparison of measured CH-layer thicknesses to the predictions of the thermochemical models. Each experimental value corresponds to the average of the full width at half maximum of two-sided Voigt distributions that are least-squares fit to the axial CH-LIF profile of all trials for each value of ϕ. The error bars represent the random uncertainty in the mean value estimated from the Student's t-distribution using a 95% confidence interval. The numerically predicted, PSF-corrected, CH layer thicknesses agree well with the experimental data for $0.8 \leqslant \phi \leqslant 1.3$, a range over which δ_{CH} values predicted by the four mechanisms generally overlap. This confirms the adequacy of the PSF-correction, even though the width of the PSF-distribution (δ_{PSF}) was derived from an independent set of CH-LIF measurements. Discrepancies between experiments and simulations are observed for methane-air and ethane-air flames at $\phi = 0.7$. LIF measurements for these two flames with low [CH] were affected by a non-negligible amount of noise that could have artificially broadened the CH layer thickness. Significant deviations among the models are noticed for $\phi \geqslant 1.3$ and the experimental values generally fall in between the predictions (except for C_4H_{10} which only has predictions from the USC and NUIG mechanisms). Given the width of the error bars, it can be concluded that the CH layer thickness is overpredicted by the SD mechanism for methane ($\phi = 1.3$), and underpredicted by GRI for ethane ($\phi = 1.3$) and propane ($1.3 \leq \phi \leq 1.5$), by USC for butane ($1.3 \leq \phi \leq 1.4$), and by NUIG for methane ($\phi = 1.3$), propane ($\phi = 1.5$) and butane ($1.3 \leq \phi \leq 1.4$).

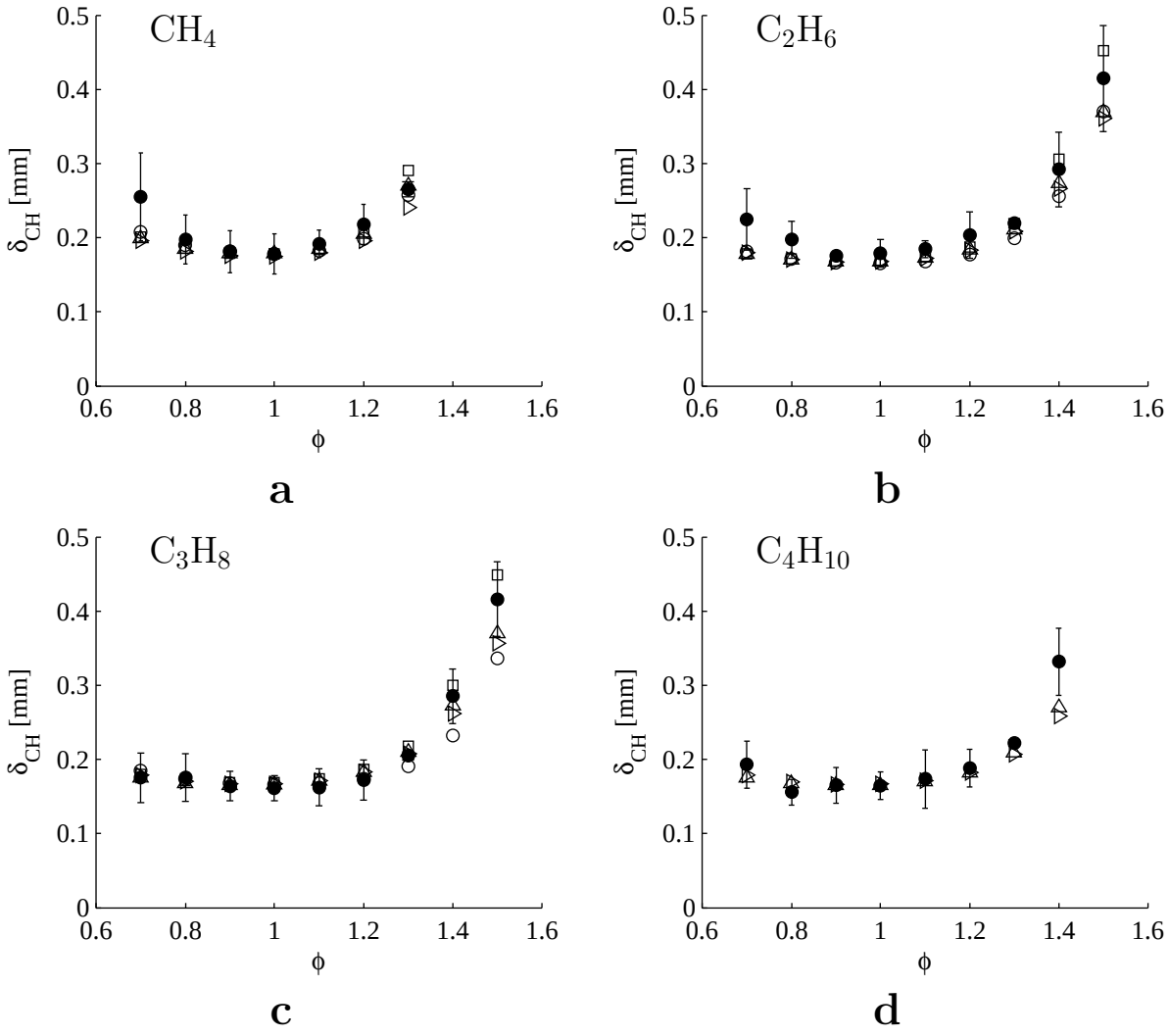

Figure 7: Measured and simulated CH profile thickness, δ_{CH}, for (a) methane, (b) ethane, (c) propane, and (d) *n*-butane flames. Same legend as Figure 5.

3.2. Analysis of variability in predictive performance of the thermochemical mechanisms

As discussed above and presented in Figure 5, the ability of currently available chemistry models at predicting CH formation is highly variable. This subsection seeks to identify the main causes of such differences, namely the order of magnitude variations in S_{LIF}/S_R. Given the complexity of modern thermochemical mechanisms, the potential sources of discrepancies are numerous, and only the most important are presented in this section. Additional information can be found in Appendix D, available online as Supplemental Material.

Figure 8 presents a simplified reaction path analysis tracking the flux of carbon through a stoichiometric, unstrained, adiabatic, freely-propagating methane-air flame. The network

was assembled by identifying the main reaction paths in the RPA diagrams produced using the output of Chemkin-Pro simulations performed with the SD, USC, GRI and NUIG mechanisms. If the contribution of all elementary reactions is included, the RPA diagram becomes so complex that it is almost unreadable. For that reason, only non-CH related pathways with $R(\mathrm{C}, s_1, s_2) > 0.01$ and CH-related pathways with $R(\mathrm{C}, s_1, s_2) > 0.001$ were considered in the analysis. The width of the arrows is scaled according to the average of the $R(\mathrm{C}, s_1, s_2)$ values of the four thermochemical mechanisms reported in Figure 9 (a), and they are coloured according to the average of the logarithmic sensitivities (L.S.) of peak [CH] to the specific rate of a given path (see Figure 9 (b)). The L.S. of a specific pathway is obtained by taking the sum of the L.S. of each individual reaction forming that path. A green (red) arrow indicates a path that upon acceleration causes an increase (decrease) in the maximum concentration of methylidyne, and vice-versa. The order of magnitude variability observed in Figure 5 must then be related to significant differences in the specific rate of the reactions making up sensitive channels; mechanisms underpredicting (overpredicting) the peak CH concentration include rates too large for paths with negative (positive) L.S. and/or too small for paths with positive (negative) L.S. It should be noted that a mechanism in reasonable agreement with a given set of experimental data may not have the most accurate chemistry. That is, it could be adjusted such that inaccuracies in the specific rate description of a sensitive path are cancelled out by tuning the rate of another sensitive path.

The RPA diagram presented here qualitatively agrees with the work of Warnatz [85] developed in more detail in [17, 84]. A hydrogen atom is initially abstracted from methane to form methyl, with the initial carbon contained in CH_4 almost completely converted to CH_3, $R(\mathrm{C}, \mathrm{CH_4}, \mathrm{CH_3}) \approx 1$. Most of the produced methyl radicals then react through the main fuel breakdown path, simplified here as the C/H/O route:

$$\mathrm{CH_3} \rightarrow \underbrace{\mathrm{CH_2O} \rightarrow \mathrm{HCO}}_{\text{C/H/O route}} \rightarrow \mathrm{CO}, \tag{7}$$

and through other pathways indirectly linking CH_3 to CH_2O via species including CH_3OH, CH_3O, and CH_2OH. The carbon passing through the C/H/O route is then discharged mainly in CO, which either escapes the control volume as is, or is transformed into CO_2 and then exhausted. A smaller, yet significant fraction of the carbon (on average about 1/6 of that

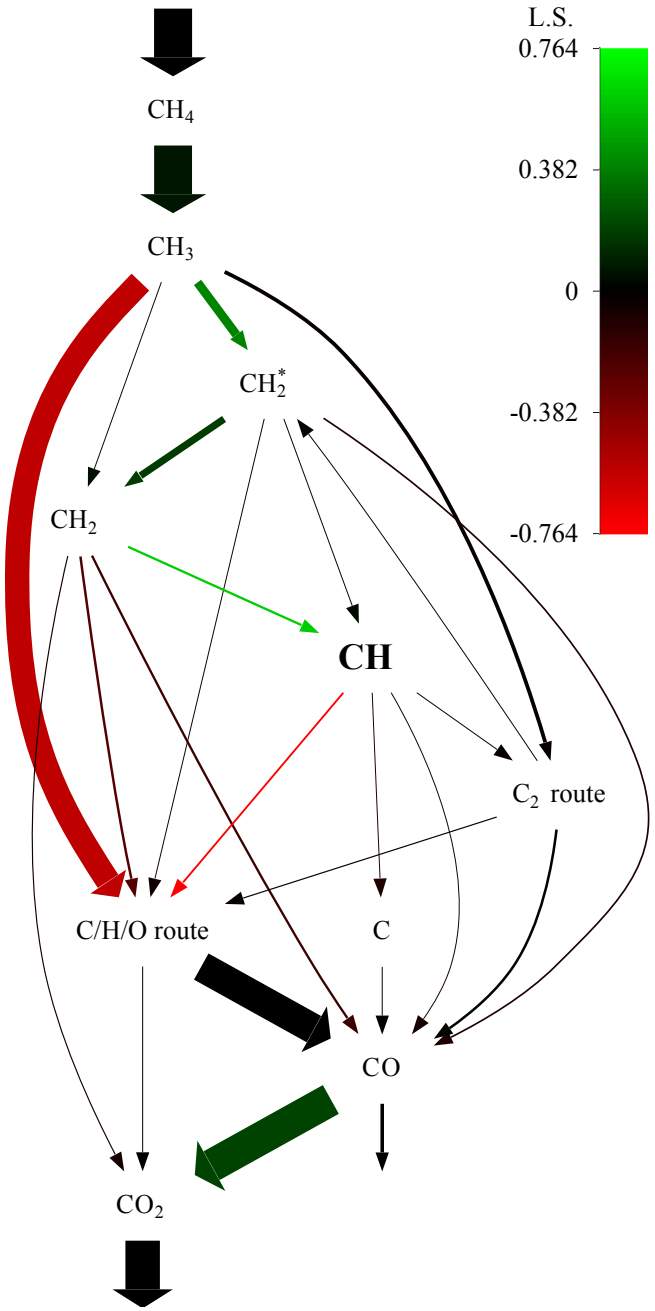

Figure 8: Simplified RPA diagram for a stoichiometric, unstrained, adiabatic, freely-propagating methane-air flame.

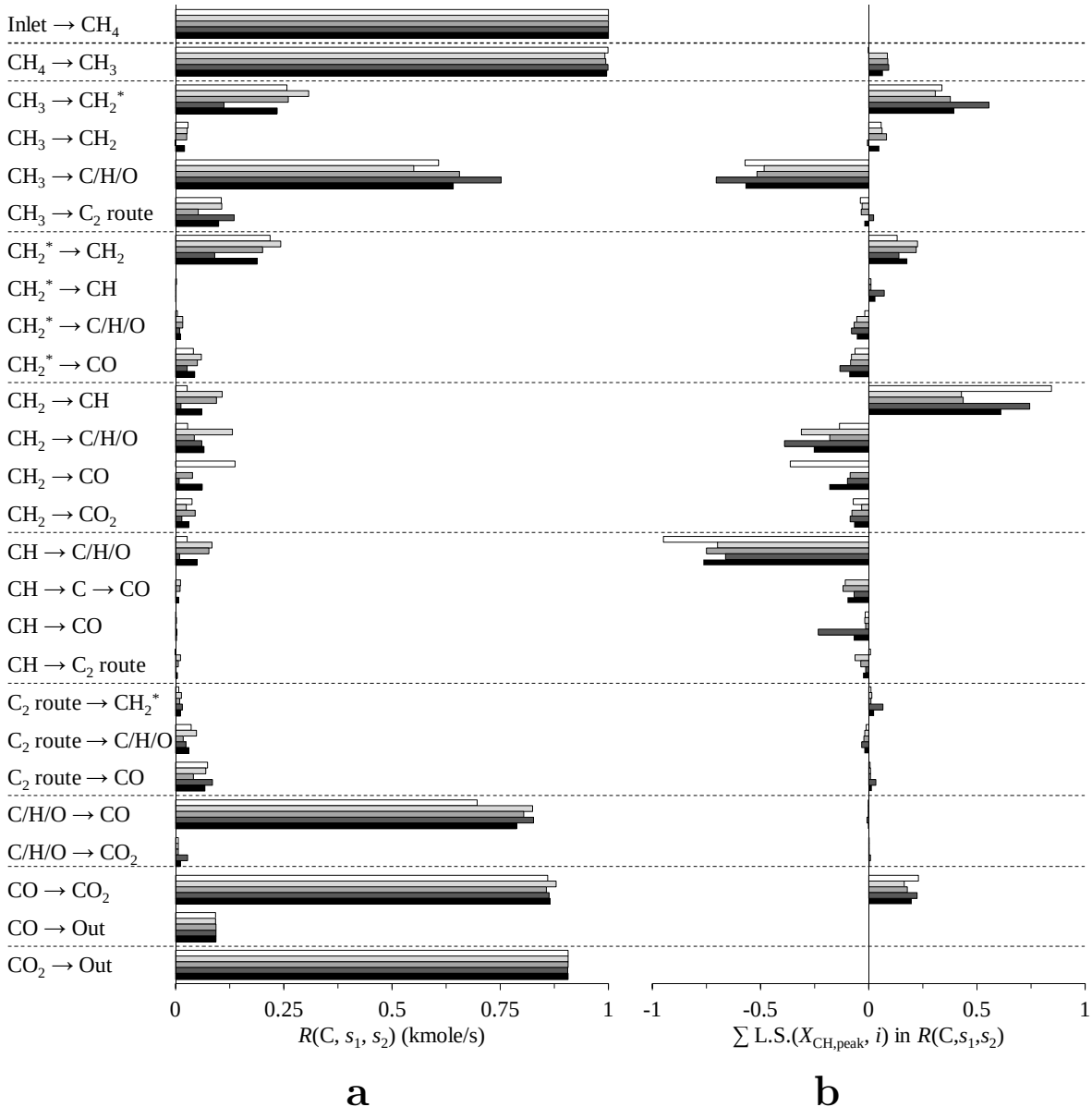

Figure 9: (a) $R(\mathrm{C}, s_1, s_2)$, and (b) $\sum_{i=1}^{\#\text{reactions}} \mathrm{L.S.}(X_{\mathrm{CH,peak}}, i)$ for the RPA diagram shown in Figure 8. Legend: □SD, □USC, ■GRI, ■NUIG, ■Average.

going in the C/H/O route) proceeds from CH_3 through a higher-order hydrocarbon route generally described as:

$$CH_3 \rightarrow \underbrace{C_2H_6 \rightarrow C_2H_5 \rightarrow C_2H_4 \rightarrow C_2H_3 \rightarrow C_2H_2 \rightarrow HCCO}_{C_2 \text{ route}} \rightarrow CO, \tag{8}$$

which, depending on the thermochemical mechanism, also includes pathways to/from C_2-oxygenated species such as CH_2CHO and CH_2CO. This carbon flowing through the C_2 route is then distributed amongst the C/H/O route, CO, and singlet-CH_2 (here labelled CH_2^*). The remaining carbon in CH_3 enters the CH-formation route presented in equation (9) via CH_2^* and CH_2, and methylidyne is consumed mainly to the C/H/O route, and to a lesser extent to C, CO, and C_2 compounds. This main CH formation route is consistent with the reaction networks presented in [33, 61, 84, 86].

$$CH_3 \rightarrow CH_2^* \rightarrow CH_2 \rightarrow CH \tag{9}$$

From Figures 8 and 9, paths flowing carbon in and out of the CH formation route have significant positive and negative L.S., respectively, particularly those directly connected to CH. The overall production rate of CH, q_{CH}, can be described by equation (10), where R_{in} and R_{out} are the numbers of reactions producing/consuming CH, $N_{r,i}$ and $N_{r,k}$ are the numbers of reactants in the reactions producing/consuming CH, k is the specific rate, $[M_j]$ is the concentration of species j, and ν is the stoichiometric coefficient. An inspection of the production and consumption rate profiles of CH, not shown here for the sake of brevity, showed that they are almost equal; at the location of maximum [CH], the overall (net) production rate represents only 2.75% of the CH rate of production. In that case, the quasi-steady-state assumption can be invoked, and the concentration profile of CH estimated according to equation (11). The presence in the numerator and denominator of the specific rate of the reactions producing and consuming methylidyne, respectively, clearly shows their direct impact on its concentration.

$$q_{\text{CH}} = \underbrace{\sum_{i=1}^{R_{\text{in}}} k_i \prod_{j=1}^{N_{r,i}} [M_j]^{\nu'_j}}_{\text{rate of production}} - \underbrace{\sum_{k=1}^{R_{\text{out}}} k_k [\text{CH}] \prod_{l=1, M_l \neq \text{CH}}^{N_{r,k}} [M_l]^{\nu'_l}}_{\text{rate of consumption}} \tag{10}$$

$$[\mathrm{CH}] \approx \frac{\sum_{i=1}^{R_{\mathrm{in}}} k_i \prod_{j=1}^{N_{r,i}} [M_j]^{\nu'_j}}{\sum_{k=1}^{R_{\mathrm{out}}} k_k \prod_{l=1, M_l \neq CH}^{N_{r,k}} [M_l]^{\nu'_l}} \tag{11}$$

CH is mainly produced through the path CH_2 to CH, which has the largest positive L.S. of the RPA. The lower plot of Figure 10(a) shows the specific rates of the two reactions making that path. The net reaction rates normalized to unity, q_{net}, obtained using the SD mechanism are also shown in the top plot to indicate the temperature range over which the reactions mostly proceed. Such additional plots will be included for informative purposes in the remainder of the paper without additional discussions. While the Arrhenius rate coefficients are exactly identical for the reaction $CH_2 + OH \leftrightarrow CH + H_2O$, there are significant discrepancies for the reaction $CH_2 + H \leftrightarrow CH + H_2$. Namely, the USC and GRI mechanisms predict specific rates approximately an order of magnitude larger than the SD and NUIG models. Comparing the rates to the recommendations of Baulch et al., the NUIG and SD mechanisms are in fair and perfect agreement, respectively, with the 1992 report [87]. However, the recommended specific rate was raised in the 2005 review [88], and the USC and GRI mechanisms are in better agreement with this revised rate. The data presented here cannot discriminate exact values for any individual reaction. However, considering the large positive L.S. for that reaction (L.S. = 0.34 on average), the discrepancies in the rates shown in Figure 10(a) must have a significant impact on the order of magnitude variability in the predictions shown in Figure 5.

Many different reactions included in the thermochemical mechanisms consume CH, and the included reactions differ from one mechanism to the other. Their sensitivity is reported in Table 2. The SD mechanism includes the fewest number of reactions, although some of the excluded ones have non-negligible L.S. values based on the other models. The USC, GRI, and NUIG mechanisms contain the same reactions, except that the latter includes the additional reaction $CH + O_2 \leftrightarrow CO + OH^*$ which presents the second-largest L.S. value. To compare the models, the rate of consumption of CH normalized by the CH concentration (denominator of equation (11)) from each mechanism is compared in the lower plot of Figure 10 (b) (note the linear scale). This normalized rate practically corresponds to an aggregated rate constant

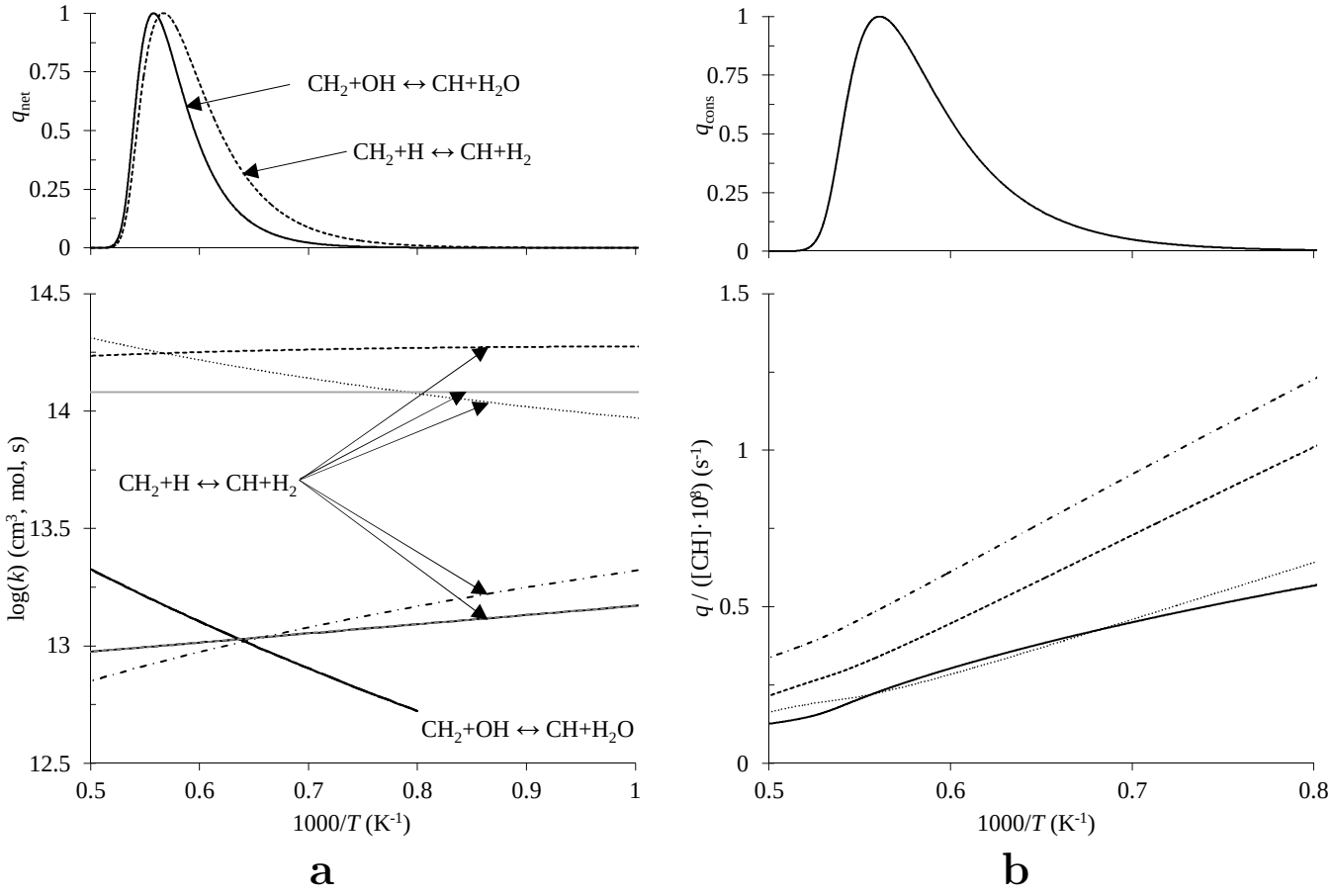

Figure 10: (a) Normalized net reaction rate (top) and specific rate (bottom) of main reactions producing CH, (b) rate of CH consumption normalized to unity (top), and normalized by the CH concentration profile (bottom). Legend: —— SD, ····· USC, - - - GRI, – · – NUIG, ------ [87], and —— [88].

independent of [CH]. The top plot of Figure 10 (b) presents the rate of consumption normalized to unity (q_{cons}) obtained using the SD mechanism. The SD and USC mechanisms are in fair agreement, while GRI and NUIG predict normalized consumption rates approximately 1.5 and 2 times higher, respectively. Considering the large negative L.S. of that pathway (see last row in Table 2), it partially explains the lower predictions of NUIG vs. SD, and GRI vs. USC.

Additionally, equation 11 shows the direct coupling between the concentrations of CH and of the reactants from which it originates. As observed in Figures 8 and 9(a), methylidyne is principally formed from CH_2. Improper description of the rates of formation and consumption of ground state (triplet) methylene results in inaccurate predictions of its concentration and, as a consequence, impacts [CH]. This dependency is highlighted by the non-negligible L.S. of

Table 2: Logarithmic sensitivities, multiplied by 10^3, of principal reactions consuming CH.

Reaction	SD	USC	GRI	NUIG
$CH + H_2O \leftrightarrow CH_2O + H$	-201	-288	-199	-455
$CH + CO_2 \leftrightarrow HCO + CO$	-45	-29	-16	-8
$CH + OH \leftrightarrow HCO + H$		-28	-18	-18
$CH + O_2 \leftrightarrow HCO + O$	-702	-354	-516	-181
$CH + O_2 \leftrightarrow CO + OH^*$				-222
$CH + O \leftrightarrow CO + H$	-15	-18	-14	-12
$CH + H \leftrightarrow C + H_2$		-108	-119	-67
$CH + CH_4 \leftrightarrow C_2H_4 + H$		-38	-27	-14
sum	-963	-863	-909	-977

the CH_2^* to CH_2, CH_2 to C/H/O route, and CH_2 to CO paths. In addition, the concentration of CH_2 is directly coupled to the concentration of its main precursor, CH_2^*. Hence, inaccuracies in the description of the rates of formation and consumption of singlet methylene cascade down the CH formation route and impact [CH]. Reactions relaxing methylene from its singlet to its triplet state, and draining carbon atoms out of the CH formation route from CH_2 and CH_2^* are numerous. Disagreements exist among the mechanisms both in terms of included reactions and their rates. However, they do not appear as the main cause of the order of magnitude variability in the predictions shown in Figure 5. Further details are provided in Appendix D, available in the Supplemental Material online, to keep this paper as succinct as possible.

Carbon flows into the CH formation route principally via the reactions $CH_3 + H \leftrightarrow CH_2^* + H_2$, and $CH_3 + OH \leftrightarrow CH_2^* + H_2O$, and bypasses it through $CH_3 + O \leftrightarrow CH_2O + H$, mostly in the forward direction. Figure 11 shows the specific rates included in the thermochemical mechanisms for these reactions. For the first reaction, the GRI, USC, and NUIG models specify the parameters in the backward direction. The ChemRev software, available from the Combustion Chemistry Centre at National University of Ireland at Galway [89], was used along with the thermodynamic properties and backward reaction rate parameters of each mechanism to obtain the forward specific rates. The USC, GRI, and NUIG mechanisms present very similar $k(T)$, while the SD model predicts a specific rate ~ 25 to $\sim 50\%$ higher. However, the L.S. obtained with the SD mechanism is 0.0366 for that reaction as it contributes only a small fraction to the CH_3 to CH_2^* path, hence reducing the impact of the higher specific rate predicted by the SD model. In contrast, the average L.S. for $CH_3 + OH \leftrightarrow CH_2^* + H_2O$ is 0.307, and significant disagreements exist among the models. The reaction mostly proceeds

in the high temperature range where the specific rates of the SD, USC and GRI mechanisms are on the same order of magnitude, although they present opposite trends with increasing temperature. On the other hand, the NUIG mechanism predicts a specific rate approximately 5.5 times lower than the other mechanisms at the location of maximum q_{net}. This is certainly an additional cause of the significantly lower $S_{\text{LIF}}/S_{\text{R}}$ predictions by the NUIG model.

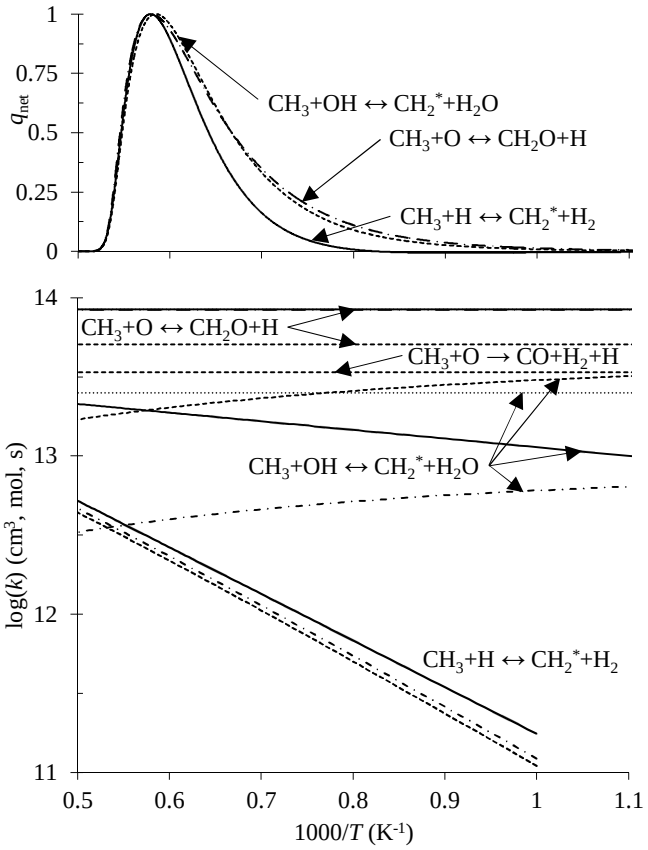

Figure 11: Normalized net reaction rate (top) and specific rate (bottom) of principal reactions consuming the methyl radical. Same legend as Figure 10.

The specific rates of the SD, USC and NUIG mechanisms for the reaction $CH_3 + O \leftrightarrow CH_2O{+}H$ agree very well, while the GRI model has $k(T)$ 40% lower than the others. However, it includes an additional reaction, $CH_3 + O \rightarrow CO + H_2 + H$ that is not present in the other mechanisms. Interestingly, the sum of the specific rate in the forward direction of both reactions in the GRI model is equal to the forward specific rate of $CH_3 + O \leftrightarrow CH_2O + H$ in the SD, USC, and NUIG mechanisms. That is, GRI bypasses carbon from the CH route at the same specific rate as the other mechanisms, but sends it to CO in addition to CH_2O. Hence, the variability in the predicted [CH] is not related to the specific rate of methyl consumption

to the C/H/O route.

It is anticipated that CH formation may also be sensitive to the thermodynamic and transport properties included in the thermochemical mechanisms. No significant disagreements were observed during our analysis, not presented here for the sake of brevity. The differences in the Arrhenius rate coefficients presented above are the principal reasons for the large variability in the mechanism predictions. Specifically, reactions $CH_2 + H \leftrightarrow CH + H_2$, $CH_3 + OH \leftrightarrow CH_2^* + H_2O$, and those consuming CH should be addressed in future combustion studies. Other pathways with lower L.S. or better agreement in terms of rate constant were not studied here, but are analyzed in Appendix D, available in the Supplemental Material. Namely, the H_2/O_2 sub-mechanism and CO to CO_2 path, both having significant L.S., were found to be fairly consistent from one mechanism to the other.

4. Conclusions

CH formation in premixed flames of C_1 to C_4 normal alkanes was quantitatively measured by linear laser induced fluorescence in jet-wall stagnation flames. This configuration provides stable, small-scale, quasi-one-dimensional flames over a wide range of conditions making them well-suited for laser diagnostics. The ability to accurately measure all necessary boundary conditions allows for direct and precise comparisons between experiments and simulations based on detailed thermochemical mechanisms. In this study, the flow velocity profile was measured by particle tracking velocimetry, and the CH concentration probed by quantitative planar laser-induced fluorescence calibrated by the Rayleigh scattering trace of nitrogen. Consistent with the methodology proposed by Connelly et al. [75], experimentally-determined ratios of CH-LIF to Rayleigh scattering signals were directly compared to simulations. The predictions of four thermochemical mechanisms (San Diego Mechanism version 2005, USC Mech version II, AramcoMech 1.3, and GRI-Mech version 3.0) were made into units compatible with the LIF measurements using a time-resolved, four-level LIF model developed in the course of the work.

The GRI mechanism yields the best overall performance over the range of fuels and equivalence ratios investigated, except for rich mixtures where SD generally has superior predictive capabilities. The AramcoMech 1.3 and San Diego mechanisms consistently underpredict, and

the USC Mech mechanism overpredicts the experimental data. Variability in the predictions over more than an order of magnitude is observed, significantly beyond the estimated errors in the measurements and the time-resolved, four-level LIF model. The thickness of the CH layer is well reproduced when the point-spread function of the imaging system is accounted for, except for the richest flames where discrepancies among the models, and against the experimental data, are noticed.

The source of the variability in the predictive performance was investigated using reaction path and sensitivity analysis. Significant differences in the specific rates are observed for reactions interacting with the CH formation route, namely $CH_2 + H \leftrightarrow CH + H_2$, and $CH_3 + OH \leftrightarrow CH_2^* + H_2O$. Furthermore, the mechanisms disagree regarding which reactions consume methylidyne, and also regarding their rate.

Accurate predictions of CH concentration are crucial as it is the principal precursor of prompt-NO formation. In order to correct the identified deficiencies in the mechanisms, a global optimization could be performed using the experimental data presented herein. Such an optimization should include all of the available kinetically-independent data in order to ensure model reliability across a wide range of combustion regimes. The set of experimental data ($S_{\mathrm{LIF}}/S_{\mathrm{R}}$) presented here is made available to chemical modellers for use as validation and optimization targets. Boundary conditions for 1D flame simulations are provided in Appendix B, and numerical values of the experimental data, as well as estimated CH concentrations, in Appendix C.

5. Acknowledgements

This work was jointly funded by the Natural Sciences and Engineering Research Council of Canada (NSERC), BioFuelNet Canada, and Siemens Canada Limited whose support is gratefully acknowledged. The authors want to thank S. Salusbury and B. Fishbein for designing and building the experimental burner, and G. Chung and J. Munzar for their help in implementing the LIF diagnostic. The authors are much obliged to J. Sutton for his advice on the Rayleigh calibration of the CH-LIF measurements.

Appendix A Time-resolved, four-level LIF model

Table A1 collects the parameters required to build the time-resolved, four-level LIF model presented in section 2.3.2. The model will be discussed and analysed thoroughly in Versailles et al. [79].

Table A1: Time-resolved, four-level LIF model parameters.

Parameter	Function	Constants				Units
		c_1	c_2	c_3	c_4	
B_{1a2a}		1.072×10^{10}				$[m^2J^{-1}s^{-1}]$
B_{2a1a}	$B_{1a2a} \cdot c_1$	0.889				$[m^2J^{-1}s^{-1}]$
I		1.34×10^{8}				$[W/m^2]$
$\Delta\nu_L$		0.34				$[cm^{-1}]$
Γ		0.583				
A_{2a1a}		6.087×10^{5}				$[s^{-1}]$
A_{2a1b}		1.209×10^{6}				$[s^{-1}]$
A_{21b}		1.770×10^{6}				$[s^{-1}]$
R_{kakb}/Q_2		2.83				
R_{kbka}	$R_{kakb} \cdot \frac{f_{B,N_{ka}}}{1-f_{B,N_{ka}}}$					$[s^{-1}]$
$f_{B,N_{1a}}$	$c_1 \cdot e^{c_2/T} + c_3 \cdot e^{c_4/T}$	0.1683	−929.0	−0.1822	−1498	
$f_{B,N_{2a}}$	$c_1 \cdot e^{c_2/T} + c_3 \cdot e^{c_4/T}$	2.608	−1402	−2.609	−1438	
τ_{cam}		30×10^{-9}				[s]
$\left(\frac{\partial\sigma}{\partial\Omega}\right)$	$f(T_R)$	ref. [81]				
T_R		296				[K]
$\tau_{\lambda,LIF}$		0.403				
$\tau_{\lambda,R}$		0.240				
δ_{PSF}		0.124				[mm]
Quenching coefficients are from [90]:						
Q_{2a1}	$\sum Q_k \cdot \frac{PX_k}{RT}$					$[s^{-1}]$
Q_{H_2}	$c_1\sigma_{H_2}T^{c_2}$	11.02	0.5			$[10^{-13}cm^3s^{-1}]$
Q_H	$c_1\sigma_H T^{c_2}$	15.09	0.5			$[10^{-13}cm^3s^{-1}]$
Q_{H_2O}	$c_1\sigma_{H_2O}T^{c_2}$	5.30	0.5			$[10^{-13}cm^3s^{-1}]$
Q_{O_2}	$c_1\sigma_{O_2}T^{c_2}$	4.79	0.5			$[10^{-13}cm^3s^{-1}]$
Q_{OH}	$c_1\sigma_{OH}T^{c_2}$	5.36	0.5			$[10^{-13}cm^3s^{-1}]$
Q_{CH_4}	$c_1\sigma_{CH_4}T^{c_2}$	5.43	0.5			$[10^{-13}cm^3s^{-1}]$
Q_{CO}	$c_1\sigma_{CO}T^{c_2}$	4.88	0.5			$[10^{-13}cm^3s^{-1}]$
Q_{CO_2}	$c_1\sigma_{CO_2}T^{c_2}$	4.59	0.5			$[10^{-13}cm^3s^{-1}]$
Q_{N_2}	$c_1\sigma_{N_2}T^{c_2}$	4.88	0.5			$[10^{-13}cm^3s^{-1}]$
Quenching cross-sections are from [90], with updates from [91]:						
σ_{H_2}	$c_1T^{c_2}e^{-c_3/T}$	6.1	0.0	686		$[Å^2]$
σ_H	$c_1T^{c_2}e^{-c_3/T}$	221	-0.5	686		$[Å^2]$
σ_{H_2O}	$c_1T^{c_2}e^{-c_3/T}$	9.6	0.0	0.0		$[Å^2]$
σ_{O_2}	$c_1T^{c_2}e^{-c_3/T}$	8.61×10^{-6}	1.64	-867		$[Å^2]$
σ_{OH}	$c_1T^{c_2}e^{-c_3/T}$	221	-0.5	686		$[Å^2]$
σ_{CH_4}	$c_1T^{c_2}e^{-c_3/T}$	52.8	-0.5	84		$[Å^2]$
σ_{CO}	$c_1T^{c_2}e^{-c_3/T}$	8.31	0.0	0.0		$[Å^2]$
σ_{CO_2}	$c_1T^{c_2}e^{-c_3/T}$	8.67×10^{-13}	3.8	-854		$[Å^2]$
σ_{N_2}	$c_1T^{c_2}e^{-c_3/T}$	1.53×10^{-4}	1.23	552.1		$[Å^2]$

Appendix B Experimental boundary conditions

The boundary conditions required to perform the quasi-1D stagnation flame simulations are presented in Table B1. Their acquisition is described in sections 2.1.1 and 2.2. The errors are given in parentheses.

Table B1: Experimentally-determined boundary conditions for stagnation flame simulations.

Fuel	ϕ	l (mm)	u_{inlet} (m/s)	$\mathrm{d}u/\mathrm{d}x\|_{\text{inlet}}$ (1/s)	T_{inlet} (K)	T_{wall} (K)
CH_4	0.7 (0.004)	11.04 (0.05)	0.258 (0.002)	50.4 (4.8)	296 (3)	316 (9)
	0.8 (0.005)	10.73 (0.05)	0.420 (0.004)	84.1 (7.0)	296 (3)	331 (10)
	0.9 (0.006)	10.87 (0.05)	0.549 (0.005)	119.2 (6.6)	296 (3)	344 (10)
	1.0 (0.006)	10.80 (0.05)	0.634 (0.006)	139.0 (4.0)	296 (3)	353 (11)
	1.1 (0.007)	11.00 (0.05)	0.613 (0.007)	145.3 (18.9)	296 (3)	353 (11)
	1.2 (0.008)	12.00 (0.06)	0.567 (0.005)	115.1 (5.8)	296 (3)	345 (10)
	1.3 (0.008)	12.80 (0.06)	0.425 (0.004)	92.9 (4.5)	296 (3)	334 (10)
C_2H_6	0.7 (0.004)	10.97 (0.05)	0.369 (0.004)	72.9 (5.7)	296 (3)	323 (10)
	0.8 (0.005)	10.99 (0.05)	0.512 (0.005)	109.8 (7.0)	296 (3)	338 (10)
	0.9 (0.006)	10.56 (0.05)	0.641 (0.006)	140.9 (7.5)	296 (3)	344 (10)
	1.0 (0.006)	10.65 (0.05)	0.730 (0.007)	167.0 (12.2)	296 (3)	363 (11)
	1.1 (0.007)	10.99 (0.05)	0.761 (0.008)	170.5 (11.8)	296 (3)	360 (11)
	1.2 (0.008)	10.76 (0.05)	0.726 (0.008)	167.8 (13.2)	296 (3)	359 (11)
	1.3 (0.008)	11.29 (0.05)	0.618 (0.006)	132.6 (6.3)	296 (3)	350 (10)
	1.4 (0.009)	12.58 (0.06)	0.454 (0.004)	91.8 (12.3)	296 (3)	336 (10)
	1.5 (0.010)	10.63 (0.05)	0.349 (0.003)	76.5 (4.0)	296 (3)	331 (10)
C_3H_8	0.7 (0.004)	10.66 (0.05)	0.367 (0.003)	74.9 (4.9)	296 (3)	324 (10)
	0.8 (0.005)	10.79 (0.05)	0.507 (0.004)	108.1 (4.3)	296 (3)	338 (10)
	0.9 (0.006)	10.76 (0.05)	0.627 (0.006)	139.4 (5.0)	296 (3)	351 (11)
	1.0 (0.006)	10.60 (0.05)	0.704 (0.006)	161.2 (7.0)	296 (3)	363 (11)
	1.1 (0.007)	10.82 (0.05)	0.727 (0.007)	169.5 (7.9)	296 (3)	361 (11)
	1.2 (0.008)	10.98 (0.05)	0.679 (0.006)	152.6 (6.9)	296 (3)	356 (11)
	1.3 (0.008)	11.43 (0.05)	0.568 (0.005)	125.5 (6.6)	296 (3)	347 (10)
	1.4 (0.009)	12.01 (0.06)	0.411 (0.004)	86.8 (5.5)	296 (3)	334 (10)
	1.5 (0.010)	12.15 (0.06)	0.289 (0.003)	55.0 (7.5)	296 (3)	323 (10)
n-C_4H_{10}	0.7 (0.004)	12.88 (0.06)	0.382 (0.003)	69.1 (3.9)	296 (3)	327 (10)
	0.8 (0.005)	12.07 (0.06)	0.512 (0.005)	104.8 (4.4)	296 (3)	341 (10)
	0.9 (0.006)	11.80 (0.06)	0.620 (0.006)	129.2 (5.0)	296 (3)	354 (11)
	1.0 (0.006)	11.01 (0.05)	0.673 (0.006)	152.5 (7.8)	296 (3)	362 (11)
	1.1 (0.007)	11.00 (0.05)	0.675 (0.006)	160.7 (6.9)	296 (3)	361 (11)
	1.2 (0.008)	10.84 (0.05)	0.625 (0.006)	141.4 (6.4)	296 (3)	357 (11)
	1.3 (0.008)	10.80 (0.05)	0.485 (0.004)	110.6 (8.3)	296 (3)	345 (10)
	1.4 (0.009)	10.10 (0.05)	0.348 (0.003)	83.5 (13.1)	296 (3)	335 (10)

Appendix C CH concentration target data

This study provides quantitative measurements of CH production in premixed flames of methane, ethane, propane and *n*-butane mixed with air. As discussed in section 2.3.1, the measured CH-LIF signal intensity is made quantitative through normalization by the Rayleigh scattering signal of nitrogen. The solutions of flame simulations performed with various thermochemical models are provided to a LIF/Rayleigh model generating numerical profiles of LIF-to-Rayleigh ratio. The maximum value of $S_{\mathrm{LIF}}/S_{\mathrm{R}}$, a scalar value selected as a surrogate measure of CH formation, is extracted from the experimental and numerical profiles and compared to assess the accuracy of thermochemical mechanisms. The benefit of this direct comparative diagnostic method is that it separates measured and simulated data in order to achieve the highest accuracy of the experimental data for the validation of thermochemical models. Table C1 presents, in numerical form, the experimental data previously presented in Figure 5.

Table C1: Measured maximum values of $S_{\mathrm{LIF}}/S_{\mathrm{R}}$. The 95% interval of confidence accounting for the scatter in the experimental data is shown in parentheses.

ϕ	CH_4	C_2H_6	C_3H_8	C_4H_{10}
0.7	0.9 (0.3)	1.8 (0.5)	1.6 (0.4)	2.6 (0.7)
0.8	2.6 (1.0)	4.3 (1.3)	5.5 (1.3)	7.2 (1.4)
0.9	5.8 (1.4)	9.0 (1.3)	10.7 (3.0)	11.3 (3.5)
1.0	11.4 (2.1)	13.0 (2.1)	15.0 (2.7)	17.9 (4.1)
1.1	14.9 (4.0)	18.3 (4.3)	24.8 (4.0)	23.5 (2.9)
1.2	16.5 (3.2)	23.3 (6.1)	25.6 (4.1)	24.2 (4.3)
1.3	11.9 (1.0)	21.0 (1.6)	23.2 (1.9)	22.6 (1.4)
1.4	—	12.2 (5.3)	15.1 (3.0)	11.5 (2.6)
1.5	—	5.5 (1.8)	6.0 (1.7)	—

To employ the direct comparative methodology, fairly accurate numerical predictions of the temperature and major species concentrations are required to generate the LIF-to-Rayleigh intensity profiles. These predictions might not be available, or sufficiently accurate, in the early stages of thermochemical model development. It is then more convenient to use concentration data as initial targets. Maximum values of methylidyne mole fraction (ppm) and concentration (mole/m^3) are presented in Tables C2 and C3, respectively. For modellers, it is also more time consuming to generate numerical profiles of $S_{\mathrm{LIF}}/S_{\mathrm{R}}$ than to compare the raw output of flame simulations to experimental data reduced to mole fractions. The data presented in Tables C2 and C3 can be used to rapidly verify the progress made in

the development of thermochemical mechanisms. However, as discussed in section 2.3.1, the highest degree of accuracy will be obtained through direct comparison of experimentally- and numerically-determined LIF intensities, the latter modelled using species and temperature profiles provided by the thermochemical mechanism under study.

Table C2: Estimated maximum mole fraction of methylidyne in premixed flames of C_1-C_4 alkanes in parts per million.

ϕ	CH_4	C_2H_6	C_3H_8	C_4H_{10}
0.7	0.2	0.3	0.3	0.4
0.8	0.5	0.9	1.1	1.5
0.9	1.4	2.3	2.5	2.8
1.0	3.2	3.8	4.1	5.0
1.1	4.5	5.7	7.3	7.0
1.2	5.2	7.5	8.0	7.4
1.3	3.5	6.5	7.1	6.7
1.4	—	3.5	4.3	3.2
1.5	—	1.4	1.6	—

Table C3: Estimated maximum number density of methylidyne in premixed flames of C_1-C_4 alkanes in mole/m^3.

ϕ	CH_4	C_2H_6	C_3H_8	C_4H_{10}
0.7	$1.2 \cdot 10^{-6}$	$2.5 \cdot 10^{-6}$	$2.1 \cdot 10^{-6}$	$3.6 \cdot 10^{-6}$
0.8	$4.0 \cdot 10^{-6}$	$7.0 \cdot 10^{-6}$	$8.6 \cdot 10^{-6}$	$1.2 \cdot 10^{-5}$
0.9	$1.0 \cdot 10^{-5}$	$1.7 \cdot 10^{-5}$	$1.9 \cdot 10^{-5}$	$2.1 \cdot 10^{-5}$
1.0	$2.2 \cdot 10^{-5}$	$2.6 \cdot 10^{-5}$	$2.9 \cdot 10^{-5}$	$3.5 \cdot 10^{-5}$
1.1	$3.0 \cdot 10^{-5}$	$3.8 \cdot 10^{-5}$	$5.0 \cdot 10^{-5}$	$4.7 \cdot 10^{-5}$
1.2	$3.3 \cdot 10^{-5}$	$4.9 \cdot 10^{-5}$	$5.3 \cdot 10^{-5}$	$4.8 \cdot 10^{-5}$
1.3	$2.2 \cdot 10^{-5}$	$4.2 \cdot 10^{-5}$	$4.7 \cdot 10^{-5}$	$4.3 \cdot 10^{-5}$
1.4	—	$2.3 \cdot 10^{-5}$	$2.8 \cdot 10^{-5}$	$2.0 \cdot 10^{-5}$
1.5	—	$9.5 \cdot 10^{-6}$	$1.0 \cdot 10^{-5}$	—

The data presented in Tables C2 and C3 were obtained by adjusting, for each fuel and equivalence ratio, the [CH] profile output by flame simulations and provided to the LIF model such that the maximum numerical LIF-to-Rayleigh ratio agrees with the experimental value. This post-processing methodology did not require new simulations. Instead, the profile of CH number density predicted by the GRI mechanism (USC for *n*-butane) was multiplied by a constant adjusted using a root-finding secant method to minimize (absolute tolerance of $1 \cdot 10^{-6}$) the error between the modelled and measured maximum values of $S_{\mathrm{LIF}}/S_{\mathrm{R}}$.

[1] R. Kee, J. Miller, G. Evans, G. Dixon-Lewis, Proc. Combust. Inst. 22 (1989) 1479–1494.

[2] T. Lieuwen, V. Yang, Gas Turbine Emissions, Cambridge Edition, 2013.

[3] J. Miller, C. Bowman, Prog. Energy Combust. Sci. 15 (1989) 287–338.

[4] C. P. Fenimore, Proc. Combust. Inst. 13 (1971) 373–380.

[5] M. Riad Manaa, D. R. Yarkony, J. Chem. Phys. 95 (1991) 1808–1816.

[6] M. Riad Manaa, D. R. Yarkony, Chem. Phys. Lett. 188 (1992) 352–358.

[7] L. Moskaleva, M. Lin, Proc. Combust. Inst. 28 (2000) 2393–2401.

[8] J. Sutton, B. Williams, J. W. Fleming, Combust. Flame 153 (2008) 465–478.

[9] P. Berg, D. Hill, A. Noble, G. Smith, J. Jeffries, D. Crosley, Combust. Flame 121 (2000) 223–235.

[10] J. Sutton, B. Williams, J. Fleming, Combust. Flame 159 (2012) 562–576.

[11] G. M. Watson, P. Versailles, J. M. Bergthorson, Combust. Flame (under review) (2015).

[12] G. M. Watson, P. Versailles, J. M. Bergthorson, (In preparation) (2015).

[13] M. Frenklach, H. Wang, M. Rabinowitz, Prog. Energy Combust. Sci. 18 (1992) 47–73.

[14] M. Frenklach, Proc. Combust. Inst. 31 (2007) 125–140.

[15] F. N. Egolfopoulos, N. Hansen, Y. Ju, K. Kohse-Höinghaus, C. K. Law, F. Qi, Prog. Energy Combust. Sci. 43 (2014) 36–67.

[16] E. Ranzi, A. Frassoldati, A. Grana, A. Cuoci, A. Faravelli, A. Kelley, C. Law, Prog. Energy Combust. Sci. 38 (2012) 468–501.

[17] C. K. Law, AIAA Journal 50 (2012) 19–36.

[18] J. Bergthorson, M. Thomson, Renew. Sust. Energy Rev. 42 (2015) 1393–1417.

[19] J. Luque, P. Berg, J. Jeffries, G. Smith, D. Crosley, J. Scherer, Appl. Phys. B 78 (2004) 93–102.

[20] J. Luque, G. Smith, D. Crosley, Proc. Combust. Inst. 26 (1996) 959–966.

[21] P. Berg, D. Hill, A. Noble, G. Smith, J. Jeffries, D. Crosley, in: 35th Aerospace Sciences Meeting, Reno, Nevada. Paper 97-0905.

[22] J. Luque, D. Crosley, Appl. Phys. B 63 (1996) 91–98.

[23] R. G. Joklik, J. W. Daily, W. J. Pitz, Proc. Combust. Inst. 21 (1986) 895–904.

[24] J. Luque, R. Klein-Douwel, J. Jeffries, G. Smith, D. Crosley, App. Phys. B: Lasers Optics 75 (2002) 779–790.

[25] J. A. Sutton, J. F. Driscoll, Appl. Opt. 42 (2003) 2819–2828.

[26] K. Walsh, M. Long, M. Tanoff, M. Smooke, Proc. Combust. Inst. (1998) 615–623.

[27] C. Gibaud, J. Snyder, V. Sick, R. Lindstedt, Proc. Comb. Inst. 30 (2005) 455–463.

[28] S. V. Naik, N. M. Laurendeau, Appl. Opt. 43 (2004) 5116–5125.

[29] M. W. Renfro, A. Chaturvedy, N. M. Laurendeau, Combust. Sci. Tech. 169 (2001) 25–43.

[30] R. Evertsen, R. Stolk, J. Ter Meulen, Combust. Sci. Tech. 149 (1999) 19–34.

[31] J. Bergthorson, D. Goodwin, P. Dimotakis, Proc. Combust. Inst. 30 (2005) 1637–1644.

[32] J. Bergthorson, Experiments and Modeling of Impinging Jets and Premixed Hydrocarbon Flames, Ph.D. thesis, California Institute of Technology, 2005.

[33] K. Schofield, M. Steinberg, J. Phys. Chem. A 111 (2007) 2098–2114.

[34] P. Bonczyk, J. Shirley, Combust. Flame 34 (1979) 253–264.

[35] P. Bonczyk, J. Verdieck, Combust. Flame 34 (1981) 253–264.

[36] J. Verdieck, P. Bonczyk, Proc. Combust. Inst. 18 (1981) 1559–1566.

[37] X. Mercier, P. Jamette, J. Pauwels, P. Desgroux, Chem. Phys. Lett. 305 (1999) 334–342.

[38] K. Peterson, D. Oh, Opt. Lett. 24 (1999) 667–669.

[39] S. Naik, N. Laurendeau, Appl. Phys. B 79 (2004) 891–905.

[40] Reaction Design, Chemkin-Pro Release 15131, 2013.

[41] D. Thomsen, N. Laurendeau, Combust. Flame 124 (2001) 350–369.

[42] U. Niemann, K. Seshadri, F. A. Williams, Combust. Flame 162 (2015) 1540–1549.

[43] R. F. Johnson, A. C. Vandine, G. L. Esposito, H. K. Chelliah, Combust. Sci. Technol. 187 (2015) 37–59.

[44] J. Bergthorson, S. Salusbury, P. Dimotakis, J. Fluid Mech. 681 (2011) 1–30.

[45] A. Eckbreth, Laser Diagnostics for Combustion Temperature and Species, Taylor & Francis, 1996.

[46] J. Daily, Prog. Energy Combust. Sci. 23 (1997) 133–199.

[47] G. Watson, J. Munzar, J. Bergthorson, Fuel 124 (2014) 113–124.

[48] G. Watson, J. Munzar, J. Bergthorson, Energy Fuels 27 (2013) 7031–7043.

[49] J. Reisel, C. Carter, N. Laurendeau, Energy Fuels 11 (1997) 1092–1100.

[50] J. Bergthorson, P. Dimotakis, Proc. Combust. Inst. 31 (2007) 1139–1147.

[51] J. D. Munzar, A. Zia, P. Versailles, R. Jiménez, B. Akih-Kumgeh, J. M. Bergthorson, in: Proc. ASME Turbo Expo 2014, Düsseldorf, Germany. Paper GT2014-25951.

[52] G. Chung, B. Akih-Kumgeh, G. Watson, J. Bergthorson, Proc. Combust. Inst. 34 (2012) 831–38.

[53] P. Versailles, J. M. Bergthorson, J. Fluids Eng. 134 (2012).

[54] F. N. Egolfopoulos, H. Zhang, Z. Zhang, Combust. Flame 109 (1997) 237–252.

[55] J. Bergthorson, P. Dimotakis, Exp. Fluids 41 (2006) 255–263.

[56] L. Benezech, J. Bergthorson, P. Dimotakis, Proc. Combust. Inst. 32 (2009) 1301–1309.

[57] G. P. Smith, D. M. Golden, M. Frenklach, N. W. Moriarty, B. Eiteneer, M. Goldenberg, C. T. Bowman, R. K. Hanson, S. Song, W. C. Gardiner, V. V. Lissianski, Z. Qin, GRI-Mech 3.0, 1999. http://www.me.berkeley.edu/gri_mech/.

[58] D. Woiki, M. Votsmeier, D. F. Davidson, R. K. Hanson, C. T. Bowman, Combust. Flame 113 (1998) 624–626.

[59] "Chemical-Kinetic Mechanisms for Combustion Applications", San Diego Mechanism web page, Mechanical and Aerospace Engineering (Combustion Research), University of California at San Diego, 2005. http://combustion.ucsd.edu.

[60] M. V. Petrova, F. Williams, Combust. Flame 144 (2006) 526–544.

[61] S. Li, F. Williams, Proc. Combust. Inst. 27 (1998) 485–493.

[62] S. Li, F. Williams, Combust. Flame 118 (1999) 399–414.

[63] H. Wang, X. You, A. Joshi, S. Davis, A. Laskin, F. Egolfopoulos, C. Law, USC Mech Version II. High-Temperature Combustion Reaction Model of H_2/CO/C_1–C_4 Compounds, 2007. http://ignis.usc.edu/USC_Mech_II.htm.

[64] W. K. Metcalfe, S. M. Burke, S. S. Ahmed, H. J. Curran, Int. J. Chem. Kinetics 45 (2013) 638–675.

[65] J. F. Grcar, M. S. Day, J. B. Bell, Combust. Theory Modell. 10 (2006) 559–579.

[66] B. Vukasinovic, M. K. Smith, A. Glezer, Phys. Fluids 16 (2004) 306–316.

[67] P. O'Brien, C. McKenna Neuman, Geomorphology 173-174 (2012) 149–160.

[68] B. Lüthi, A. Tsinober, W. Kinzelbach, J. Fluid Mech. 528 (2005) 87–118.

[69] T. Echekki, M. Mungal, Proc. Combust. Inst. 23 (1991) 455–461.

[70] L. Benezech, Premixed hydrocarbon stagnation flames: Experiments and simulations to validate combustion chemical-kinetic models, Engineer's thesis, 2008.

[71] Y. Ju, C. K. Law, Proc. Combust. Inst. 28 (2000) 2913–2920.

[72] S. Salusbury, J. Bergthorson, Combust. Flame In Press (2015).

[73] C. J. Sung, C. K. Law, R. L. Axelbaum, Combust. Sci. and Tech. 99 (1994) 119–132.

[74] C. J. Sung, J. S. Kistler, M. Nishioka, C. K. Law, Combust. Flame 105 (1996) 189–201.

[75] B. Connelly, B. Bennett, M. Smooke, M. Long, Proc. Combust. Inst. 32 (2009) 879–886.

[76] J. Luque, D. Crosley, LIFBASE Database and Spectral Simulation Program (Version 1.6), Technical Report MP 99-009, SRI International, 1999.

[77] E. Rea, A. Chang, R. Hanson, J. Quant. Spectrosc. Radiat. Transfer 37 (1987) 117–127.

[78] V. Vasudevan, R. Hanson, C. Bowman, D. Golden, D. Davidson, J. Phys. Chem. A 111 (2007) 11818–11830.

[79] P. Versailles, G. M. Watson, A. C. Lipardi, J. M. Bergthorson, In preparation (2016).

[80] N. L. Garland, D. R. Crosley, Appl. Opt. 24 (1985) 4229–4237.

[81] J. Sutton, J. Driscoll, Opt. Lett. 29 (2004) 2620–2622.

[82] E. Hecht, Optics - 3rd edition, Addison-Wesley, 1998.

[83] R. Adrian, C. Yao, App. Optics 24 (1985) 44–52.

[84] C. K. Law, Combustion Physics, Cambridge University Press, New York, NY, United States, 2006.

[85] J. Warnatz, Proc. Combust. Inst. 18 (1981) 369–384.

[86] K. Schofield, Energy Fuels 26 (2012) 5468–5480.

[87] D. L. Baulch, C. J. Cobos, R. a. Cox, C. Esser, P. Frank, T. Just, J. a. Kerr, M. J. Pilling, J. Troe, R. W. Walker, J. Warnatz, J. Phys. Chem. Ref. Data 21 (1992) 411.

[88] D. Baulch, C. Cobos, C. Bowman, R. Cox, J Phys. Chem Ref. Data 34 (2005) 757–1397.

[89] S. Rolland, J. M. Simmie, Int. J. Chem. Kinet. 37 (2005) 119–125.

[90] M. Tamura, P. Berg, J. Harrington, J. Luque, J. Jeffries, G. Smith, D. Crosley, Combust. Flame 114 (1998) 502–514.

[91] M. Renfro, K. Venkatesan, N. Laurendeau, Proc. Combust. Inst. 29 (2002) 2695–2702.